

Review

Recent Advances in CoSe_x and CoTe_x Anodes for Alkali-ion Batteries

Yuqi Zhang, Zhonghui Sun , Dongyang Qu , Dongxue Han  and Li Niu 

College of Chemistry and Chemical Engineering, Guangzhou University, Guangzhou 510006, China; 2112105042@e.gzhu.edu.cn (Y.Z.); dxhan@gzhu.edu.cn (D.H.); lniu@gzhu.edu.cn (L.N.)

* Correspondence: cczhsun@gzhu.edu.cn (Z.S.); dyqu@gzhu.edu.cn (D.Q.)

Abstract: Transition metal selenides have narrow or zero band-gap characteristics and high theoretical specific capacity. Among them, cobalt selenide and cobalt telluride have some typical problems such as large volume changes, low conductivity, and poor structural stability, but they have become a research hotspot in the field of energy storage and conversion because of their high capacity and high designability. Some of the innovative synthesis, doping, and nanostructure design strategies for CoSe_x and CoTe_x , such as CoSe-InCo-InSe bimetallic bi-heterogeneous interfaces, CoTe anchoring MXenes, etc., show great promise. In this paper, the research progress on the multistep transformation mechanisms of CoSe_x and CoTe_x is summarized, along with advanced structural design and modification methods such as defect engineering and compositing with MXenes. It is hoped that this review will provide a glimpse into the development of CoSe_x and CoTe_x anodes for alkali-ion batteries.

Keywords: CoTe_x ; CoSe_x ; anodes; alkali-metal-ion batteries



Citation: Zhang, Y.; Sun, Z.; Qu, D.; Han, D.; Niu, L. Recent Advances in CoSe_x and CoTe_x Anodes for Alkali-ion Batteries. *Coatings* **2023**, *13*, 1588. <https://doi.org/10.3390/coatings13091588>

Academic Editor: Je Moon Yun

Received: 1 August 2023

Revised: 6 September 2023

Accepted: 8 September 2023

Published: 12 September 2023



Copyright: © 2023 by the authors. Licensee MDPI, Basel, Switzerland. This article is an open access article distributed under the terms and conditions of the Creative Commons Attribution (CC BY) license (<https://creativecommons.org/licenses/by/4.0/>).

1. Introduction

The demand for clean renewable energy sources such as wind and solar power has increased due to the energy problems and environmental pollution from traditional fossil energy. Lithium-ion batteries (LIBs) were born as high-performance energy storage devices to compensate for the inconvenience of storing clean energy [1,2]. Today, lithium resources are increasingly scarce; thus, sodium-ion batteries (SIBs) and potassium-ion batteries (PIBs) have become two of the hopes to solve the problem of resource shortage [3,4]. The prerequisite for further application of sodium/potassium-ion batteries is to prepare negative electrode materials with appropriate working voltage, excellent cycling performance, and high energy density. Anode materials can be divided into three types: intercalation type (e.g., carbon [5] and TiO_2 [6]), alloy type (Si, Ge, Sb [7], etc.), and conversion type (Co_3O_4 [8], Fe_xS [9], etc.). Although an intercalated anode has a stable structure and good electrochemical cycling stability, it still has the disadvantages of low energy density and limited specific capacity. In addition, the alloy-type anode has a high capacity, but the large volume change caused by the alloy reaction brings the disadvantage of poor stability. Compared with the former two, the conversion negative electrode has a reasonably high specific capacity and a small volume expansion, making it a potential choice for ion batteries' anodes [10].

In recent years, transition metal chalcogenides (TMCs) have been widely studied as representative conversion-type anode materials due to their stable performance, high theoretical specific capacity, abundant natural resources, diverse types, and low cost. They hold great potential in meeting the demand for high-energy-density anodes in alkali-ion batteries [11]. Compared to transition metal sulfides, transition metal selenides exhibit higher volumetric capacity as anionic battery anodes. Additionally, the weaker M-Se bond compared to M-O and M-S bonds improves the reaction kinetics of transition metal selenides, resulting in higher energy density and electronic conductivity. Moreover, transition metal selenides have larger interlayer spacing, which helps alleviate volume expansion issues during cycling, especially for larger alkali metal ions such as sodium and potassium.

Therefore, they possess advantages in electrochemical energy storage applications [12–17]. Compared to transition metal oxides and sulfides, transition metal tellurides possess lower electronegativity, the highest conductivity, and the highest volumetric capacity. They are typical layered materials with a large interlayer space, which is beneficial for rapid ion transport in electrodes. This results in excellent electrode wetting and ion diffusion kinetics. So far, many selenides (such as CoSe_x [18], ZnSe_x [19], MoSe_x [20], and FeSe_x [21]) and tellurides (e.g., NiTe_x [22], FeTe_x [23]) have been studied as ion battery anode materials.

Cobalt-based materials have become important materials in various fields (such as hydrodesulfurization and hydrodefluorination) due to their unique catalytic activity, electrochemical performance, and ferromagnetism [24–26]. Among them, LiCoO_2 is one of the most successful commercial cathode materials for lithium-ion batteries (LIBs) [27]. Based on the success of LiCoO_2 , research on Na_xCoO_2 as a cathode material for sodium-ion batteries has also been widely conducted [28]. In terms of anode materials, cobalt has various oxidation states, and cobalt-based chalcogenides have diverse types and high theoretical sodium storage capacity, making them highly favored by researchers. Cobalt-based composite anodes, such as cobalt oxide [29], cobalt phosphide, and cobalt–aluminum alloys, have theoretical capacities of 700–1000 mAh g^{-1} , which is 2–3 times that of graphite anodes. They have diverse crystal structures and low cost, receiving increasing attention in recent years. Among them, CoSe_x is widely used as an anode material for alkali-ion batteries due to its large capacity, strong conductivity, and weak electronegativity [18,30–34]. CoTe_x is considered to be a potential choice with excellent electrochemical performance in terms of metallicity, magnetism, electronics, and electrocatalysis [35]. In the past few years, extensive research has shown that cobalt selenides and tellurides can be used as potential anodes with high capacity or improved rate performance. However, their inherent volume changes as conversion anodes, relatively low electronic conductivity, and side reactions can lead to significant reversible capacity loss and low active material utilization. Recently, various energy storage batteries have been working on mitigating these issues and have achieved successes, such as forming hybrid/composite samples to enhance conductivity, optimizing electrode design and electrolyte content, and adjusting voltage windows [31].

At present, some progress has been made in the research of energy storage and conversion of transition metal selenides and tellurides—typically cobalt-based compounds [36]. However, it is necessary to study the application and reaction mechanisms of cobalt selenide and cobalt telluride in the three types of metal-ion battery in a timely and systematic manner. This paper reviews the recent progress in the preparation and application of $\text{CoSe}_x/\text{CoTe}_x$ -based electrodes (Figure 1). The electrode design and reaction mechanism are introduced in detail. Finally, the challenges and opportunities in this field are presented (Figure 2). This review will significantly advance the research on innovative $\text{CoSe}_x/\text{CoTe}_x$ design to improve its application in energy storage devices.

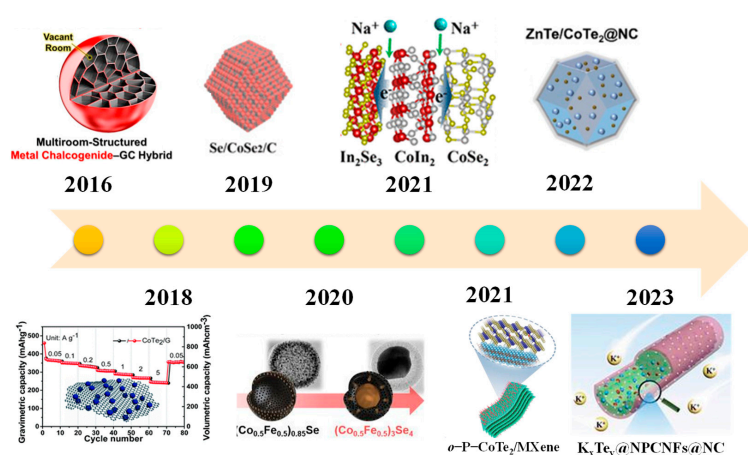


Figure 1. Typical recent advances in the synthesis of $\text{CoSe}_x/\text{CoTe}_x$ -based electrodes, Refs. [37–45].

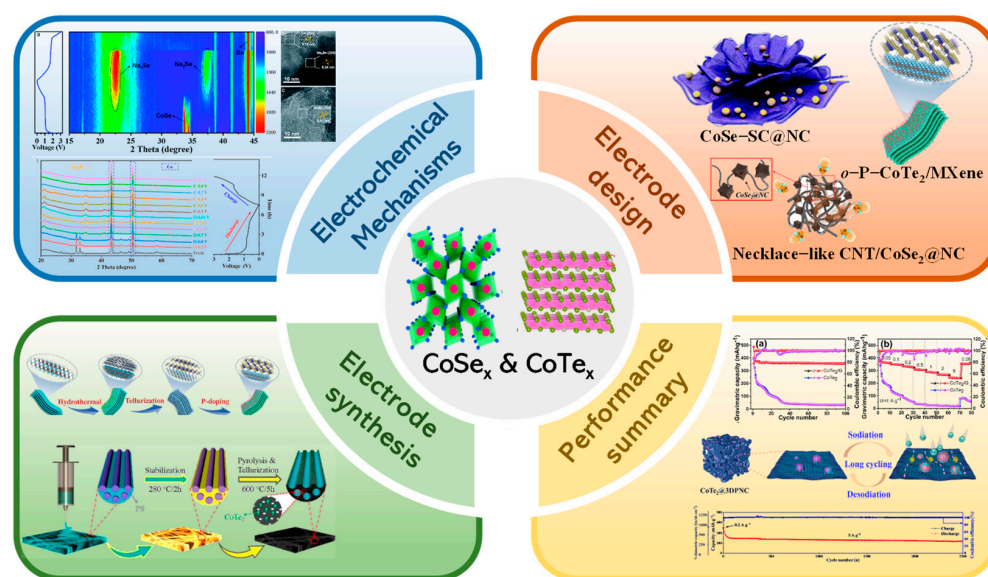
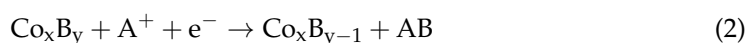


Figure 2. This paper summarizes from four perspectives, including electrochemical mechanisms, electrode design, synthesis, and performance; Refs. [38,42,46–48].

2. Electrochemical Reaction Mechanisms

As anode materials during charging and discharging processes, different metal-based compounds usually have different kinds of reactions, such as intercalation, conversion, and alloying. For example, intercalation–conversion–alloying reactions take place during the charging and discharging of Sn- and Sb-based compounds; Mo-, W-, Fe-, and Ni-based compounds mainly have intercalation and conversion reactions, while Nb-based compounds only have intercalation reactions [49]. The metal-based anode affects its reaction type. TMCs with conversion reactions can accommodate more alkali ions through the multi-electron transfer process and have a higher capacity. In addition, the combination with chalcogenide elements is conducive to the conversion reaction during the charge–discharge process. Due to the weak TM–B (B = Se and Te) bonds, TMBs have a high theoretical capacity, as well as excellent electrical conductivity and convenient ion transport channels. Co_xB_y has been used as a potential anode in alkali-ion batteries. The storage mechanism between Co_xB_y in LIBs/SIBs/PIBs is the conversion reaction that eventually generates Co and A_xB (A = Li, Na, K). In particular, a few intermediate reactions may occur during the Co_xB_y discharge processes, as shown in the following equations:



Deciphering the electrochemical reaction mechanism of CoSe_x and CoTe_x is significant to enhance their application in batteries. The latest progress on the reaction mechanisms of cobalt selenide and cobalt telluride for the anode material of LIBs, SIBs, and PIBs is summarized below.

2.1. CoSe_x

Many types of research on the storage mechanisms of CoSe_x anodes have been conducted. Among them, the storage path of CoSe_x in PIBs is different from that in SIBs and LIBs. Yu et al. [34] studied the potassium-ion storage mechanism of octahedral CoSe_2 nanotubes threaded with N-doped carbon through first-principles calculation (Figure 3a–f). The calculation showed that the formation energies of CoK_xSe_x were all positive, indicating that the insertion of K^+ into CoSe_2 is difficult to achieve, and it is more inclined to replace Co to generate K_2Se . The reason for this is that potassium atoms are too large to penetrate

the lattice of CoSe₂, whereas the non-stoichiometric selenide CoSe_{1-x} (Co₃Se₄) has a wider lattice than CoSe₂, achieving K⁺ embedding. The actual reaction process can be explained as follows:

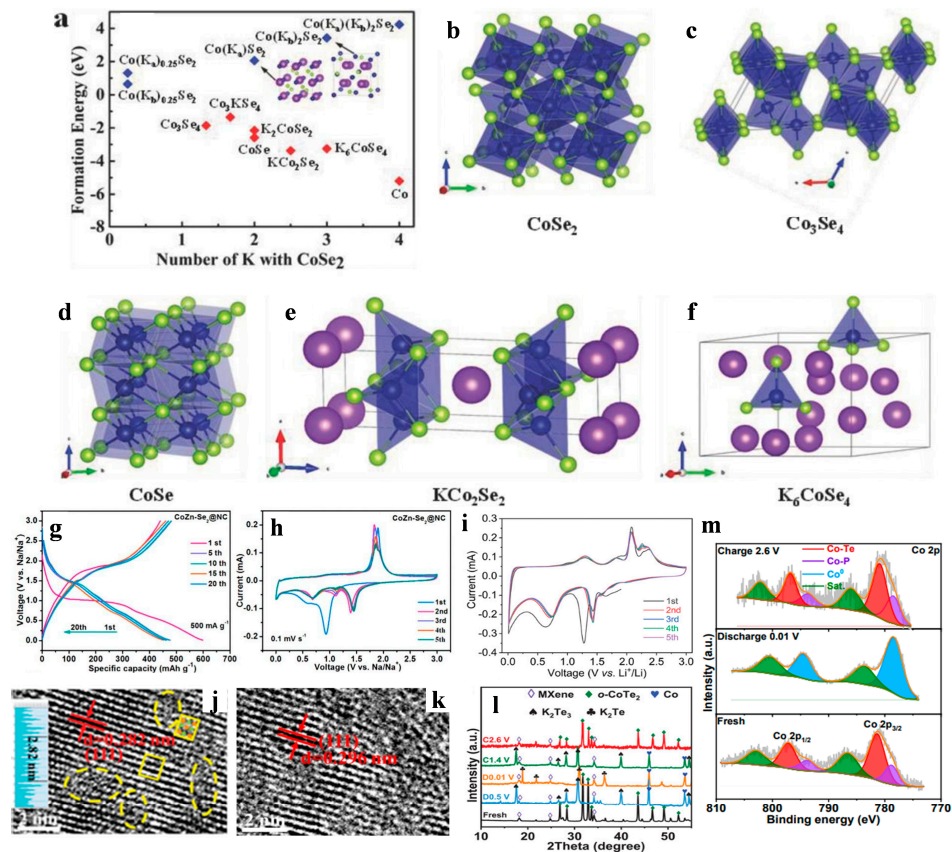
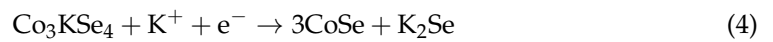
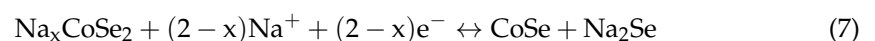
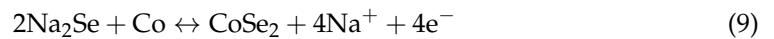
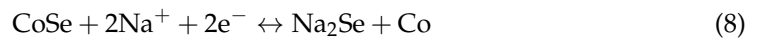


Figure 3. (a) The formation energy of conversion products. (b–f) Schematic molecular structures using in this work; Ref. [34]. (g) The cycling performance and (h) CV curve; Ref. [50]. (i) CoSe/G CV curve; Ref. [51]. (j) HRTEM for o-P-CoTe₂/MXene and (k) after discharging to 1.0 V. (l) Ex situ XRD and (m) ex situ XPS Co 2p; Ref. [38].

In contrast to PIBs, Jiang et al. [50] found the appearance of three new peaks in cyclic voltammetry (CV) curves (Figure 3h), indicating that CoSe₂ turns into Na_xCoSe₂, CoSe, and Co. The oxidation peaks at 1.53 V and 1.89 V represent the intermediate product Na_xCoSe₂ and CoSe₂, which is the fully charged product during the charge process, respectively. The locations of these peaks are highly consistent throughout the five cycles of reduction and oxidation, together with the corresponding position of the charging and discharging platform (Figure 3g), testifying to the reversibility of the charge–discharge process. The actual reaction mechanism can be summarized as follows:



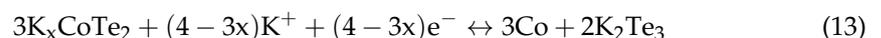


In LIBs, Jiang et al. [51] found three prominent peaks of CoSe/G at 1.42, 1.27, and 0.63 V in the first cathodic scan through the first five CV curves in LIBs (Figure 3i). Li^+ inserted into the CoSe showed a prominent peak at 1.42 V, corresponding to the formation of Li_xCoSe . The solid–electrolyte interphase (SEI) formed at 1.27 V. The wide peak at 0.63 V can be ascribed to the conversion reaction from Li_xCoSe to Li_2Se and Co. The anode peaks at 1.28 and 2.1 V signify the oxidation reactions that convert Li_2Se and Co into CoSe. The reaction process of CoSe anode in LIBs can be expressed as follows:



2.2. CoTe_x

As an emerging potential anode, the storage mechanism of CoTe_x is being extensively studied. Xu et al. [38] performed high-resolution transmission electron microscopy (HRTEM), X-ray diffraction (XRD), and X-ray photoelectron spectroscopy (XPS) analyses on CoTe_2 nanowires with a Te vacancy (o-P- $\text{CoTe}_2/\text{MXene}$) in different discharge and charge states to study the potassium storage behavior. When the half-cell discharged to 1.0 V, the HRTEM (Figure 3j) showed that the lattice spacing of the (111) plane expanded significantly to 0.296 nm compared with the initial state (Figure 3k, 0.282 nm), which proves the existence of K^+ intercalation above 1.0 V. At 0.5 V, peaks of K_2Te_3 and Co were observed in the ex situ XRD spectra (Figure 3l). This observation confirmed the conversion reaction from CoTe_2 to Co and K_2Te_3 . After further discharging to 0.01 V, a peak of K_2Te was observed, indicating that K_2Te_3 was further converted into the final reduction product (K_2Te). When the half-cell was charged to 1.4 V, K_2Te converted to K_2Te_3 and Co. When the anode was further charged to 2.6 V, the peak of o-P- $\text{CoTe}_2/\text{MXene}$ reappeared. Ex situ XPS (Figure 3m) spectra further confirmed that the peak of Co $2p^{3/2}$ continued to shift from 781.4 eV to 778.4 eV during complete discharge, corresponding to the formation of Co. Therefore, the o-P- $\text{CoTe}_2/\text{MXene}$ anode conversion mechanism in PIBs can be described by the following reactions:



Recently, Li et al. [41] published a more detailed supplement on the storage mechanism of CoTe_x in PIBs. As shown in the in situ XRD pattern (Figure 4a), after discharging to 1.21 V, the peak of CoTe_2 shifted to a lower angle, indicating that K^+ was embedded into the CoTe_2 lattice and K_xCoTe_2 formed. Upon further discharging to 0.01 V, the peak of CoTe_2 became weaker, corresponding to the conversion of CoTe_2 to Co and K_xTe_y . When charged to 3 V, the peak of CoTe_2 reappeared. In situ XPS analysis (Figure 4b) showed that the metallic Co phase appeared in the high-resolution Co 2p spectrum when the cell was discharged to 0.8 V. In the Te 3d spectrum, K_5Te_3 appeared, indicating that K_xCoTe_2 was converted to K_5Te_3 at 0.8 V. When discharging to 0.4 V, the cobalt peak strengthened and a new peak of K_2Te appeared in the Te 3d spectrum. Upon further discharging to 0.1 V, K_5Te_3 was almost transformed into K_2Te . The electrochemical reaction mechanism was further studied by transmission electron microscope (TEM), energy-dispersive X-ray spectroscopy (EDS), and HRTEM (Figure 4c–h). The TEM and EDS patterns proved that the structure remains stable and the elements are evenly distributed after the cycle. The

discharge HRTEM image shows the (100) crystal plane of Co, the (251) crystal face of K_5Te_3 , and the (311) and (200) crystal faces of K_2Te (Figure 4d). In addition, upon full charge, the (011) plane of $CoTe_2$ (Figure 4g) appears, which is consistent with the in situ XRD results. In summary, the above results show that K_xCoTe_2 converted totally to K_5Te_3 , and then K_5Te_3 converted to K_2Te during the discharge process, and the authors clearly express the evolution of polytellurides in Figure 4i. Therefore, the relevant reversible reactions are summarized below:

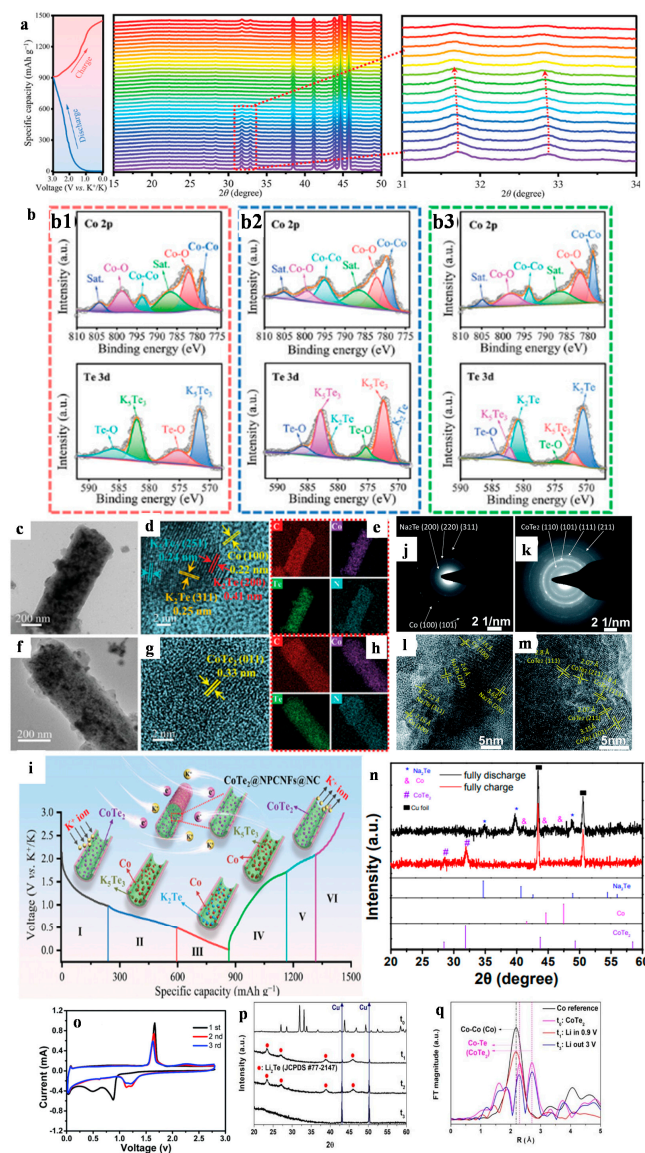
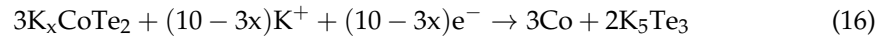
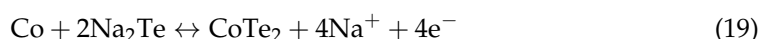


Figure 4. (a) In situ XRD patterns. (b) XPS of Co 2p and Te 3d at discharged state of (b1) 0.8 V, (b2) 0.4 V, and (b3) 0.1 V. (c,f) TEM, (d,g) HRTEM, and (e,h) EDS images at 0.1 V and 3 V, respectively. (i) Schematic diagram of the PIB storage mechanism of the $CoTe_2@NPCNFs@NC$; Ref. [41]. $CoTe_2/G$ (j,k) SAED patterns, (l,m) HRTEM, and (n) ex situ XRD at 0.01 V and 2.8 V in the first cycle. (o) CV curve; Ref. [42]. (p) Ex situ XRD. (q) EXAFS after Li-embedded/Li-detached; Ref. [52].

Zhang et al. [42] clarified the sodium-ion storage mechanism of CoTe₂ by selected-area electron diffraction (SAED, Figure 4j–k), HRTEM (Figure 4l–m), and ex situ XRD (Figure 4n). At the end of discharge, the peaks of Co and Na₂Te could be clearly observed from the ex situ XRD pattern. Moreover, the signals of Co and Na₂Te could be detected in the SAED pattern. The crystal lattice of Na₂Te and Co also appeared in HRTEM. After charging to 2.8 V, the CoTe₂ phase peak could be collected again. A clear CoTe₂ ring was observed in the SAED diagram. At the same time, Zhang analyzed the storage mechanism of Na ions from the CV curve (Figure 4o). A reduction peak formed at about 0.83 V, because CoTe₂ formed Co nanocrystals and Na₂Te with Na ions. The oxidation peak at about 1.65 V can be ascribed to the reformation of CoTe₂. It can be summarized as follows:



Ganesan et al. [52] studied the deep material changes of CoTe₂ cycling in LIBs by ex situ XRD (Figure 4p) and extended X-ray absorption fine structure (EXAFS, Co-K-Edge, Figure 4q). In the XRD pattern, when discharging to 0.9 V, it can be seen that the peak of CoTe₂ changed to the peak of Li₂Te, and CoTe₂ also changed to Co in EXAFS, which means that the conversion reaction in the discharge process is that CoTe₂ changes to Co and Li₂Te. Finally, although no recovery of CoTe₂ was observed in the XRD pattern at a full charge of 3.0 V, the main CoTe₂ EXAFS peak reappeared, confirming the reversibility of the material. Based on the experimental results, the LIB conversion mechanism for CoTe₂ is proposed as follows:



It is known that many works have fully studied the reaction mechanisms of cobalt selenide and cobalt telluride in LIBs, SIBs, and PIBs. Many in situ and ex situ analytical characterization methods have emerged. In situ XRD, XPS, and ex situ TEM, HRTEM, etc., can well demonstrate the mechanisms of CoSe_x and CoTe_x. However, due to emerging anode design methods such as doping and heterojunction, heteroatoms and conductive carbon materials will bring various synergistic effects to cobalt selenide and cobalt telluride. At present, the mechanistic analysis of cobalt selenide and cobalt telluride anodes mainly focuses on the reaction between alkali ions and CoSe_x or CoTe_x. In fact, the analysis of the synergistic mechanism between substances in the anode requires more in-depth research, and at the same time, innovative research methods need to be developed.

3. Electrode Design

As conversion-type anodes, CoSe_x and CoTe_x can bring enthralling high weight/volume capacity due to multiple electron transfer processes. However, due to the low conductivity of the converted anode materials and the large volume change in the process of intercalation/deintercalation, their practical application has been hindered. Therefore, effective strategies to solve these problems have been explored through carbon recombination [53], core-shell structures [54], defect engineering [55], etc.

Two approaches used to modify cobalt selenides and cobalt tellurides are the introduction of defects (e.g., point defects and heterogeneous interfaces) and structural design. Point defects like vacancies and dopings can interfere with surrounding atoms, resulting in lattice distortion, forming a good adjusted electronic structure with improved conductivity and diffusion coefficients [56]. The inorganic heterostructure of the anode builds an interfacial electric field as a facilitative transport channel, resulting in rapid Li/Na/K ion reaction kinetics. Considering the excellent prospects of interface engineering, Dong et al. [57] realized a “structural function motifs” design in a ZnO/ZnS anode. The ZnO/ZnS heterostructure regulates the state around the Fermi level, narrowing the band gap and, thus, improving the electronic conductivity. The introduction of defect engineering can create synergistic effects that alter the inherent properties of materials, unlike structural design

and composite strategies [58,59]. In addition, Co 3d electrons with the low spintronic structure $t_{2g}^6 e_g^1$ are known to produce a Jahn–Teller effect in CoSe_2 [60]. Proper doping of metal ions can alleviate Jahn–Teller distortion to a certain extent [61,62] and promote a more stable electrode structure and better cycling stability. Defect engineering is widely used in CoSe_2 and has also been reported in recently emerging CoTe_2 materials.

In addition to defects, structural designs such as core–shell structures or CoSe_x and CoTe_x composite carbon materials [42] can take advantage of carbon’s high conductivity and deformation resistance, not only reducing the risk of electrode crushing but also improving the rate performance. The latest reports of introducing defects or innovative structural designs to CoSe_x and CoTe_x are summarized below.

3.1. Introducing Defects

The modification methods of defect engineering include entry-point defects and surface defects. In recent studies, the introduction of point defects has been divided into metallic elements and non-metallic elements. Secondly, surface defects generally introduce heterogeneous structures. Recent advances in the combination of the above engineering with cobalt selenide and cobalt telluride are summarized below.

3.1.1. Doping with Metal Elements

Due to the large volume variation during circulation, the structural solidity and circulation function of metal selenides are weak, which limits the feasibility of their application. To overcome the above problems, some studies have prepared polyselenide metal nanostructures by adding inert elements [63]. The activity of the transition-metal-based materials can further be improved through coupling with other metals and non-metals [64]. The reason for the excellent doping performance of metal atoms is that the introduction of two or more metal atoms into a mixed-metal selenide results in the formation of more multicomponent selenides. Some studies have shown that this result can significantly improve the electrical conductivity of discharge products and further provide a buffer matrix to adapt to the expansion stress [65]. They benefit from strain relief and spectacular pseudocapacitance effects, thus reducing the energy barrier for ionic diffusion and showing considerable improvement in electrochemical performance.

For the voltage window of CoSe_2 , previous studies have usually shortened it to 0.5–3.0 V to stabilize the reversible capacity of long cycles [66,67]. Ji et al. [50] doped a variety of metal ions such as Ni^{2+} and Cu^{2+} into nitrogen-doped carbon-shell-coated CoSe_2 particles to solve the problem of capacity loss caused by shortening the window. The doped product $\text{CoM-Se}_2@\text{NC}$, obtained by carbonizing a bimetallic zeolite imidazole skeleton (ZIFs) precursor, had more outstanding capacity than $\text{CoSe}_2@\text{NC}$ at 0.01–3.0 V. It was shown that the long cycle stability of CoSe_2 can be optimized effectively and the inefficient cycle caused by window adjustment can be eliminated under the synergistic action of the participation of another metal ion and the N-doped carbon shell.

Lu et al. [68] introduced Mo into a CoSe_2 self-supported nanosheet array ($\text{Mo-CoSe}_2@\text{NC}$) and investigated the performance of Mo in SIBs. In the XPS diagram (Figure 5a–b), the 3d spectrum of Mo consisted of peaks at 232.3 eV and 235.4 eV, associated with the characteristic spin-orbital bistates of $\text{Mo } 3d^{5/2}$ and $3d^{3/2}$, respectively, which implies that Mo^{6+} ions enter the CoSe_2 lattice [69]. The embedded Mo defect in the CoSe_2 lattice not only produced more redox sites, but also induced the generation of mixed phases of o- CoSe_2 and c- CoSe_2 , as evidenced by the coexistence of two hybrid phases of CoSe_2 in the SAED diagram (Figure 5d).

Wang [70] formed FeCo–Se in situ on a carbon cloth, and this multilayer array was able to provide sufficient active surfaces and shuttle channels for sodium ion exchange, thereby achieving excellent electrochemical kinetics. XRD (Figure 5g) proved that after the Co–Se was doped with Fe, impurities such as cobalt oxide, iron oxide, iron selenide, and FeCo alloy were not produced, implying that Fe ions only enter the Co–Se lattice. Notably, when more than 50% iron salt was added to the Co–Se material, the morphology of Fe–Se changed

from a layered nanosheet array into pyramidal particles (Figure 5e–f), with a decline in electrochemical performance.

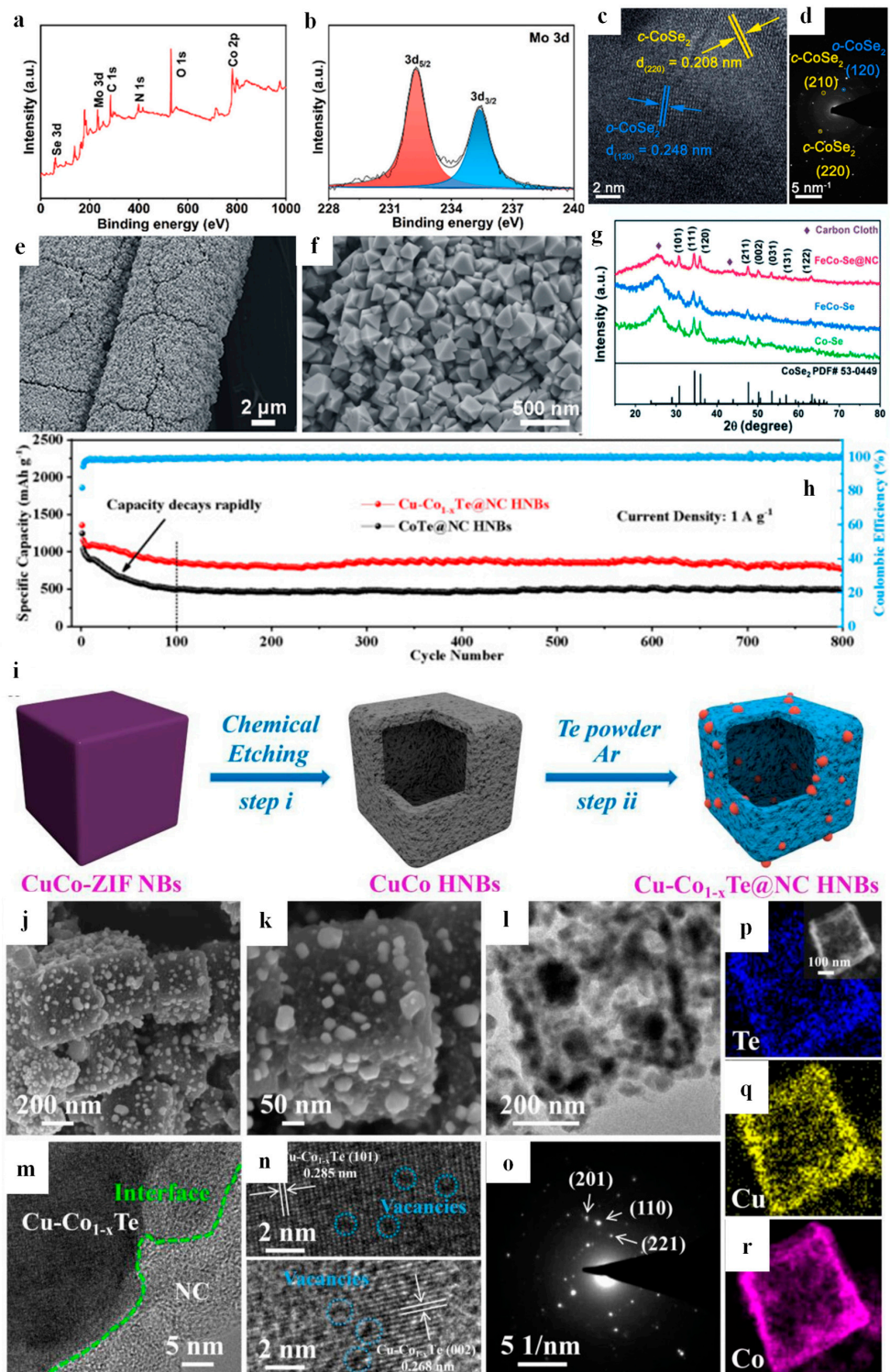


Figure 5. XPS of Mo–CoSe₂@NC with (a) survey and (b) Mo 3d. (c) HRTEM and (d) SAED; Ref. [68]. (e,f) Typical low- and high-magnification SEM (scanning electron microscope) images and (g) FeCo–Se XRD; Ref. [70]. (h) Li-ion batteries’ performance. (i) Schematic representation of the synthesis of Cu–Co_{1-x}Te@NC HNBs with (j–l) SEM and TEM images, (m,n) HRTEM images, and (o) SAED pattern and (p–r) elemental mappings, Ref. [71].

3.1.2. Doping with Non-Metallic Elements

For cobalt telluride, Hu et al. [71] prepared Cu-doped cobalt telluride hollow carbon nanocells (Cu-Co_{1-x}Te@NC HNBS, Figure 5j–l) by chemically etching CuCo-ZIF nanocells and tellurizing them (Figure 5i). The copper–cobalt tellurium was homogeneously embedded in the nanobox (Figure 5p–r), and Co vacancies were constructed by copper induction (Figure 5n). At the same time, the interaction in the heterogeneous interface between nitrogen-doped carbon and cobalt telluride (Figure 5m) triggered the transfer of the p-band to interface charge transfer, so that the composite exhibited faster ion and electron diffusion kinetics than HNB electrodes, contributing to improved storage performance of lithium-ion batteries (Figure 5h).

Doping with non-metallic elements, especially chalcogenide elements, can not only produce polysulfides with alkali ions to improve the storage capacity, but also induce vacancy formation like metal elements to form a built-in electric field. Yu [34] reported an octahedral CoSe₂ sawtooth chain array threaded with N-doped carbon nanotubes (NCNTs) as a high-performance PIB anode. Highly conductive NCNTs form a flexible conductive network that greatly accelerates electron transfer and improves rate performance. Nitrogen-doped NCNTs also provide additional capacity to CS-NCNTs, constituting a versatile composite carbon material.

Wang [33] prepared Co_{0.85}Se_{1-x}S_x nanoparticles by using S, which is of the same family as Se, as a point doping tool. The sample was formalized in a metal–organic framework, carbonized in graphene and, finally, cured in situ. Density functional theory (DFT) proved that S doping enhanced the adsorption energy of Co to alkali metal ions (Figure 6a–h). The hollow polyhedral skeleton of the double-carbon shell (Co_{0.85}Se_{1-x}S_x@C/G) with a stable structure and S vacancies reduced the volume change, increased the number of electrochemical active sites, and improved the alkali-ion storage performance.

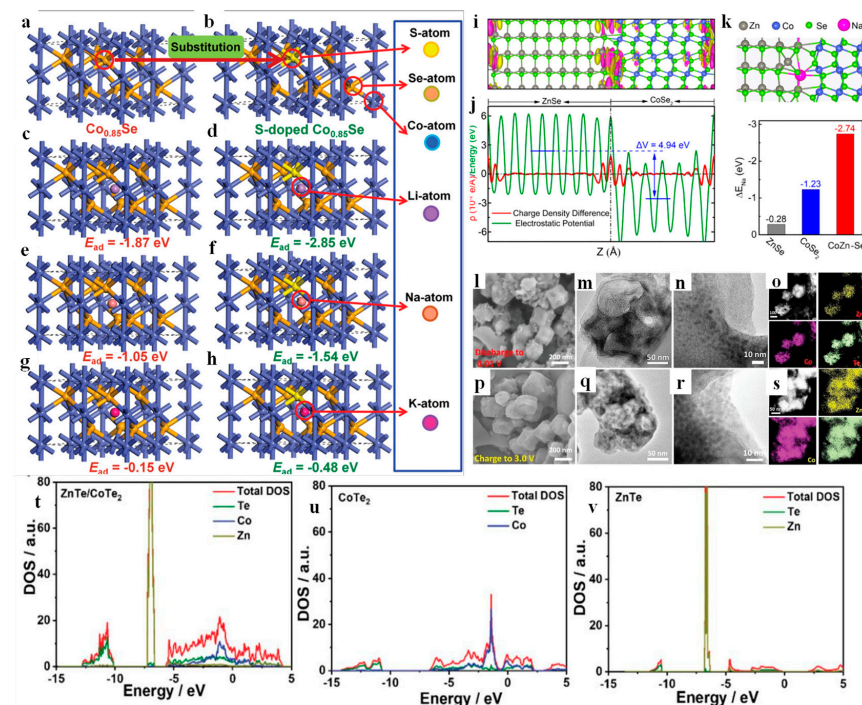


Figure 6. (a–h) DFT in crystal structures and alkali-ion adsorption sites for (a,c,e,g) Co_{0.85}Se and (b,d,f,h) S-doped Co_{0.85}Se; Ref. [33]. (i) The differential charge density between CoSe₂ and ZnSe in the phase boundary is calculated. (j) Averaged electrostatic potential. (k) The Na atom adsorption energy of ZnSe, CoSe₂, and CoZn–Se; Ref. [72]. (l–o) SEM, TEM, HRTEM, and EDS images, respectively, for a ZnTe/CoTe₂@NC anode at 0.01 V and (p–s) 3.0 V. (t–v) Total density of states (TDOS) for CoTe₂, ZnTe, and ZnTe/CoTe₂, respectively; Ref. [40].

Moreover, given the high conversion capacity of phosphorus, Ye et al. [73] reported in another work that P was successfully doped into CoSe₂. It was found through P 2p spectroscopy that additional Co-P and P-Se bonds could be generated by P doping, which could enhance the structural stability of CoSe₂. Xu [38] also used P to induce Te vacancies in o-CoTe₂ nanowires. Compared with h-CoTe₂, the Co 2p and Te 3d peaks of o-CoTe₂ showed significantly higher binding energy on the XPS images after P doping. EPR showed that the characteristic Te vacancy signal of o-P-CoTe₂/MXene was stronger and wider, indicating that the vacancy content increased significantly. Brunauer–Emmett–Teller (BET) theory showed that P doping increased the specific surface area. These results show that Te vacancy defects and P doping not only provide the active sites but also jointly enhance the structural stability of CoTe₂.

3.1.3. Heterojunctions

Heterostructure refers to the geometric structure and connecting interface formed by the combination of two or more materials through physical or chemical methods [74,75]. In the heterojunction, electrons will transition from a high Fermi level to a low Fermi level, resulting in potential difference due to interfacial polarization at the heterojunction [76] and the internal electric field. The existence of the internal electric field effect is helpful to accelerate the diffusion of metal ions and increase the adsorption energy of ions [77,78]. In addition, lattice distortion and charge redistribution taking place at heterogeneous boundaries can not only improve charge-transfer efficiency and conductivity, but also provide additional active sites for reversible redox reactions [79,80]. Therefore, due to the active role of the heterogeneous interface, heterogeneous anodes can obtain a stable nanostructure and excellent storage performance [81]. Therefore, in view of problems such as the low conductivity and large volume expansion of chalcogen-based metal materials, it is considered to be an effective strategy to construct high-quality heterogeneous structural interfaces to improve their storage performance [82].

Previously, Fang [72] reported a bimetallic selenide heterogeneous structure (CoSe₂/ZnSe@C) for SIBs. The phase-boundary charge redistribution of Co/Zn was studied by theoretical calculation. The Na⁺ adsorption energy showed that the ZnSe side had a phase boundary with high electron density, which was more conducive to the adsorption of Na⁺ ions, accelerating the ion movement and charge conduction, and achieving high reaction kinetics and high electrical conductivity (Figure 6i–k). In addition, the multistep conversion reaction in the Co/Zn heterostructure can effectively relieve the stress of Na⁺ insertion. CoSe₂/ZnSe@C also showed good OER (oxygen evolution reaction) activity, providing additional evidence that the Co/Zn heterogeneous interface accelerated the redox reaction.

Xiao [83] recently also reported a similar application of heteroselenides in SIBs. He developed ZnSe/CoSe₂-CN heterostructures with Se vacancies via controllable in situ selenization. HETEM images showed a clear heterogeneous interface between ZnSe and CoSe₂, which can create electric fields to promote the movement of ions and electrons. Electron paramagnetic resonance (EPR) spectra showed an obvious signal caused by the selenium vacancy trapping electrons at $g = 2.003$, confirming the presence of the Se vacancy in the sample. The more induced active sites and the enhanced electronic conductivity introduced by the Se vacancy can improve the electrochemical properties of the materials.

Analogously, Zhang et al. [40] reported a template-assisted strategy to achieve in situ formation of a bimetallic tellurium heterostructure (ZnTe/CoTe₂@NC) on N-doped carbon shells. The results showed that both the electron-rich Te sites and the internal electric fields generated by electron transfer from ZnTe to CoTe₂ in Te heterojunctions provided rich cation-adsorption sites and promoted interfacial electron transport during the potassic/de-potassic process. Notably, as Zn led to ZIF-8 crystal formation, with the introduction of Zn²⁺ species into Co-ZIF-67, Zn²⁺ ions acted like an obstacle to Co-ZIF-67 crystals' nucleation and growth. Concretely, Zn delays the Co-ZIF-67 nucleation dynamics, thus resulting in relatively small doping particle sizes. The growth of ZIF-67 dominated by Co leads to the production of larger crystals in the reaction–diffusion

process [84,85]. The finer ZnTe/CoTe₂ nanoparticles prepared by the heterojunction method showed higher structural stability. Ex situ SEM, HRTEM, and EDS were performed on the cycled ZnTe/CoTe₂@NC (Figure 6l–s). The ZnTe and CoTe₂ nanoparticles kept their original appearance, with no obvious particle aggregation. In addition, the TDOS results presented in Figure 6t–v highlight the discontinuous band gap of Fermi levels and confirm the semiconductor properties. In contrast, ZnTe/CoTe₂ has an obvious hybridization zone in the conduction band, resulting in significantly higher TDOS of ZnTe/CoTe₂ than that of both ZnTe and CoTe₂. This indicates that the electronic conductivity of ZnTe/CoTe₂ is significantly improved.

In addition to zinc–cobalt heterojunctions, He et al. [86] chose Ni to produce coral-like Ni_xCo_{1–x}Se₂ for the first time using a layered structure. The introduction of Ni formed a hierarchical structure to prevent structural fragmentation, accelerated the electron transmission, and shortened the Na⁺ diffusion path. Zhu et al. [87] used the carbonization and subsequent selenization process design to encapsulate Ni₃Se₄@CoSe₂@C/CNTs in a core–shell three-dimensional interpenetrating two-carbon frame. Ni₃Se₄@CoSe₂ was evenly dispersed into a three-dimensional carbon skeleton structure/carbon nanotube network, greatly enhancing the conductivity and further achieving fast Na⁺ diffusion.

3.2. Structural Design

Nanomaterials, especially spherical and small nanocrystals, have their isotropic physical properties, large active surface, and high packing density [88–90]. More active sites can be exposed by delicate structures (e.g., sea urchin CoSe₂ [88], CoSe microspheres [91]). By using carbon coatings, CoSe_x and CoTe_x can be well maintained in nanoform and improved in terms of cycling stability by using constraint effects (such as CoSe-C@C [92] and o/h-CoTe₂ [93]). Combination with structural carbon can produce interfacial interactions, which can effectively improve diffusion kinetics, electrical conductivity, and structural compatibility, thus achieving excellent electrochemical performance [10,94]. For example, three-dimensional conductive carbon network structures with large channels can provide diffusion paths, improve the migration rate of ions in the battery material, and reduce the limitation of poor conductivity of CoSe_x and CoTe_x [66]. Metal–organic frameworks (MOFs) possess exceptionally high surface area and porosity, allowing for the adsorption and storage of gases, liquids, and even small molecules. This property makes them promising for applications such as energy storage, separation, and catalysis. Moreover, by optimizing the composite structure, the electrochemical properties of the composites can be further improved, and the volume strain of the active nanomaterials in the carbon matrix can be reduced. Therefore, carbon materials such as reduced graphene oxide (rGO) and MXenes are not only electrically conductive but also have good ductility, which can greatly enhance the structural compatibility of CoSe_x and CoTe_x anode materials.

However, MOFs, MXenes, and other carbon-based materials have their limitations. For example, MOFs are prone to acid–base interference and structural collapse. MXene etching processes can be complex and hazardous. Additionally, low energy density is a common drawback of these materials. Therefore, recently, researchers have been consolidating the carbon-based structure of transition-metal-based MOFs through annealing and synthesizing high-performance ion battery anodes using vapor-phase methods [95]. High-capacity ion battery anode materials can be obtained through green etching of MXenes using only grinding and annealing via molten salt methods [96]. These structural design approaches are frequently employed in the design of cobalt selenide and cobalt telluride anodes. The latest progress in combining the abovementioned methods with cobalt selenide and cobalt telluride for alkali-metal-ion battery cathodes is summarized below.

3.2.1. Freestanding Electrodes

Common electrodes are made of an active material composited with a binder and conductive carbon on the current collector, and the presence of the binder and collector fluid especially affects the energy density. Therefore, the development of freestanding

electrode structures to increase the proportion of active materials and eliminate the negative effects of the binder is a promising direction [97].

Electrospinning is used to produce individual electrode materials, allowing the active material to be embedded in a network of carbon fibers. The carbonized material can be cut so as to be used as an electrode, avoiding mechanical losses caused by mixing adhesives with conductive materials and coatings [98,99]. Self-supported electrodes can alleviate electrode pulverization and construct interwoven electron/ion transport networks, thus improving electrochemical energy storage performance.

Zhan et al. [47] innovatively prepared a self-supported cobalt telluride electrode for SIBs. They synthesized $\text{CoTe}_2@\text{NMCNFs}$ via electrospinning and subsequent in situ tellurization (Figure 7a–f). Material characterizations revealed NMCNFs with N-doped active sites and porous carbon networks with high specific surface area. These positive effects promote electrolyte penetration and mitigate the aggregation effect in the CoTe_2 nanoparticles by reducing the volume changes during the cycle (Figure 7g–j). The long cycle of $\text{CoTe}_2@\text{NMCNFs}$ shows a high reversible Na^+ storage capacity, long-term cycle stability, and high rate capacity. In general, the overall conductivity of the electrode is greatly improved, and Na^+ diffusion is promoted, thanks to the strong three-dimensional crosslinked composite fiber and the absence of voluminous inactive components.

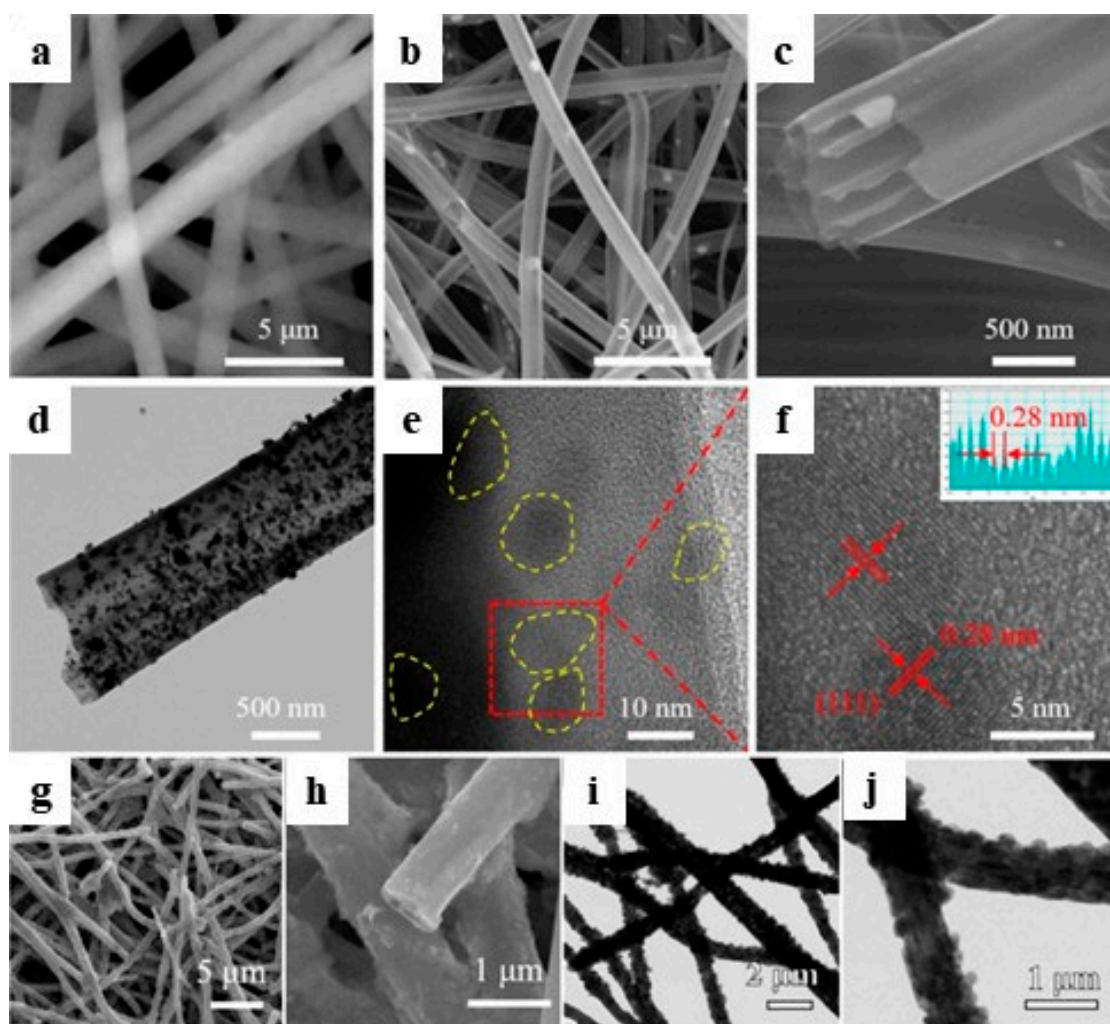


Figure 7. (a–c) SEM and (d–f) TEM images of PAN/PS/Co(ac)₂·4H₂O. (g,h) SEM and (i,j) TEM images of $\text{CoTe}_2@\text{NMCNFs}$ after 300 cycles at 200 mA g⁻¹. Ref. [47].

Meanwhile, Park et al. [100] prepared cobalt selenite (p-CoSeO₃-CNF) embedded in carbon composite nanofibers by electrospinning. Among them, the heat-treated nanofibers containing cobalt and selenium formed CoSe₂ nanocluster intermediates. Then, through the final oxidation step, CoSe₂ was converted to amorphous CoSeO₃. Part of the carbon fiber was changed into CO₂ gas during the oxidation process, leaving pores and forming mesopores in the nanofibers. The carbon and pores limited the volume change of CoSeO₃ during repeated sodification/desodification processes, allowing the electrolyte to permeate easily and reducing the diffusion path of sodium ions. The large network carbon structure accelerated electron transport, and the high performance of p-CoSeO₃-CNF was demonstrated. Electrospinning has also been reported for SIB and LIB anode materials other than CoSe₂ [32,101].

3.2.2. Carbon-Cloth-Based Electrodes

Commercially available carbon cloth (CC) material, consisting of hundreds of fibers woven tightly together, ensures that the fibers are interconnected and can be rolled into different shapes without compromising their integrity [102]. The stable cycling performance of CC-based electrodes makes them a competitive option for industrial applications of metal-ion batteries [103].

According to the different raw materials, carbon fiber is mainly divided into three substrates: asphalt-based carbon fiber, PAN-based carbon fiber, and viscose-based carbon fiber. PAN-based carbon fiber is rich in raw materials and superior to the other two types. Therefore, PAN-based carbon fiber is the most widely used, accounting for more than 90% [104]. The difference between the growth of active substances in PAN-based carbon cloth and the embedding of active substances in electrospinning is that carbon cloth generally penetrates active substances into existing carbon substrates via infiltration methods, hydrothermal methods, and other methods. However, electrospinning uses PAN, solvent, and metal salt to dissolve directly into the active material. Both have their advantages, such as the toughness of carbon cloth and the advantage of electrospinning for in situ doping treatments, which can enhance the synergistic effects of carbon nanowires and active substances [105].

To date, carbon cloth combined with active substances has been used in fuel cells [106], catalysis [107], lithium–sulfur batteries [108,109], supercapacitors [102], etc. There have also been some studies on carbon cloth combined with metallic chalcogenide compounds as negative electrodes for LIBs [110]. For cobalt selenide, Wang et al. [70] grew FeCoSe on carbon cloth, and Lu et al. [48] synthesized Mo-doped CoSe₂ nanosheets, proving that the carbon cloth and cobalt selenide have a good synergistic effect and are more conducive to the formation of bimetallic synergies (Figure 8). However, cobalt telluride combined with carbon cloth as a negative electrode for LIBs, SIBs, and PIBs has rarely been reported.

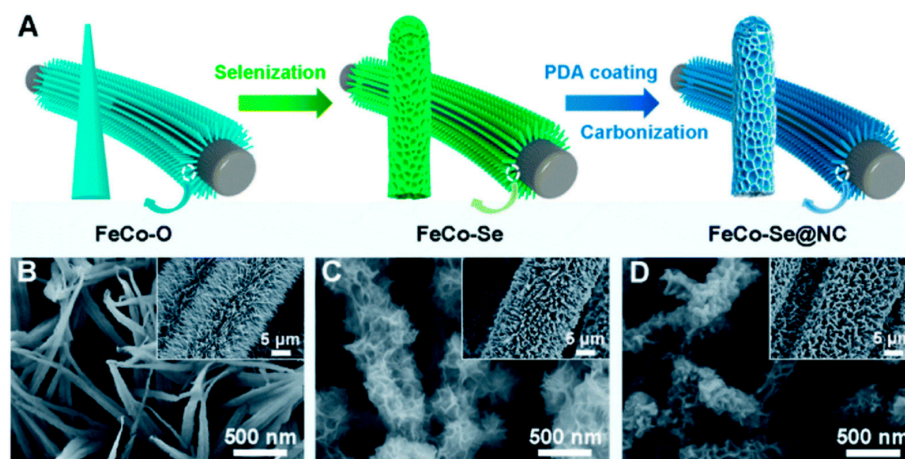


Figure 8. (A) Synthesis of FeCo-Se@NC and (B–D) SEM images of the material in each step; Ref. [68].

3.2.3. MOF-Based Electrodes

MOFs with a high specific surface area and adjustable pore structure are widely used in the fields of calcification and energy conversion due to their stable structure, large specific surface area, and diverse functions [95,111,112]. Under appropriate conditions, MOFs can be used as precursors and/or templates to derive metal chalcogenides with regular topography and excellent electrochemical properties (Figure 9) [113–115]. Notably, MOFs have proven to be ideal templates for the preparation of transition metal selenides and tellurides. In recent reports, it has been shown that transition metal selenide and telluride nanocrystals can be embedded 1–3D porous carbon substrates to form efficient conductive networks [116]. In addition, the relatively high surface area and large pores of the high-dimensional conductive substrate enhance the wettability of the electrolyte to the material and promote ion diffusion, thereby improving the storage performance [117]. Therefore, MOFs as a template for the preparation of nanoscale electroactive materials and porous carbon matrix hybrid structures have broad application prospects.

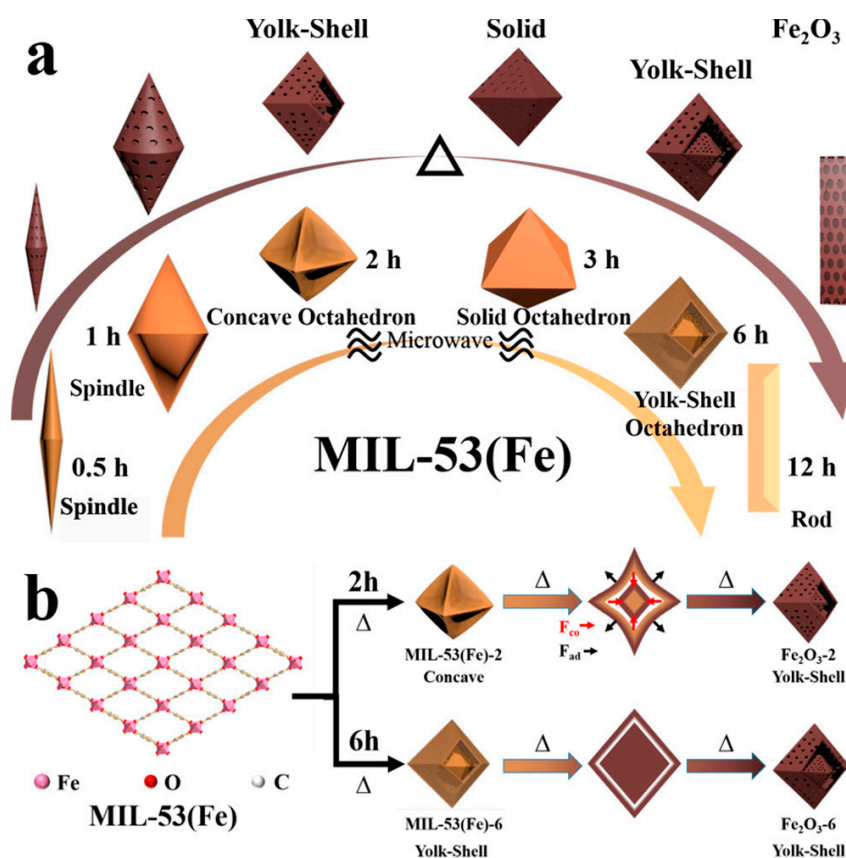


Figure 9. Transition metals have various valence states and can form various complex structures, such as Fe-based MIL-53 with yolk-shell octahedron morphologies: (a) process of MIL-53(Fe) growth and (b) the formation process of Fe₂O₃-2 and Fe₂O₃-6; Ref. [115].

More recently, Xiao [39] prepared hollow In₂Se₃/CoSe₂ nanorods by growing Co-ZIF-67 on the surface of In-MIL-68 and via in situ selenization. During selenization, selenium atoms penetrate from the surface of the nanorod to the inside, while indium atoms diffuse outward in opposite directions and at different speeds, creating the Hilken–Dahl effect and forming hollow structures [118]. At the same time, the mass ratio of ZIF-67 to MIL-68 grown on the surface was studied by changing the concentration of cobalt nitrate. The results showed that the ZIF-67 nanoparticles became smaller and could be uniformly deposited on the surface of MIL-68 with the decrease in the concentration of cobalt nitrate in solution (Figure 10).

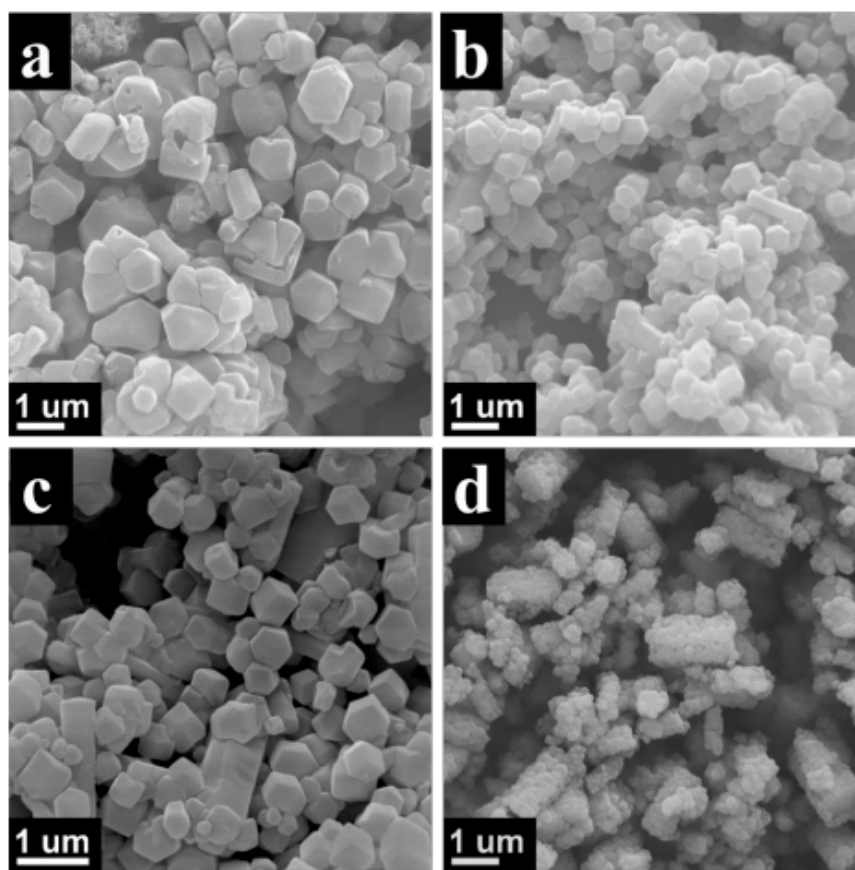


Figure 10. SEM images of In-MOF: $\text{Co}(\text{NO}_3)_2$ = (a) 1:8, (b) 1:6, (c) 1:4, and (d) 1:3; Ref. [39].

Wang et al. [119] prepared cobalt selenide (CoSe_2 -CNS) anchored on carbon nanosheets by selenizing cobalt embedded in 1D-MOF carbon nanosheets (Co-CNS). CoSe_2 grown in situ on carbon nanosheets showed close contact between CoSe_2 and carbon. At the same time, CoSe_2 -CNS also has typical two-dimensional structural characteristics, which are conducive to electrolyte penetration and ion/electron transport. In addition, the carbon matrix can alleviate the volume expansion of CoSe_2 during the desodification process. As the result of these advantages, CoSe_2 -CNS provides a stable cycle capacity of 468 mA h g^{-1} , together with a high rate capability of 352 mA h g^{-1} at $10,000 \text{ mA g}^{-1}$.

3.2.4. MXene-Based Electrodes

MXenes, which include transition metal carbides or carbon nitride, have proven to be novel materials with great potential for energy storage [120,121]. MXenes have high electrical conductivity, large interlayer spacing, and excellent mechanical properties, enabling them to act as a fluid collector and buffer deformation at the same time [122]. Their electrical and electronic properties can be customized through modifications to the MXenes' functional groups, solid solution structures, or stoichiometry to meet the needs of different scenarios [123]. As a result, titanium carbide has demonstrated outstanding catalytic activity and selectivity as a co-catalyst in various catalytic reactions, finding wide applications in energy conversion, environmental protection, and organic synthesis [124].

Xu [38] used P-induced o- CoTe_2 nanowires to anchor MXene nanosheets (o-P- CoTe_2 /MXene). The elastic MXene formed a tight interfacial interaction with P- CoTe_2 (Figure 11). DFT calculations further showed that the new superstructure had higher electronic conductivity, enhanced the adsorption capacity of K^+ ions, and reduced the energy barrier to ion diffusion. Meanwhile, the entire battery was cycled through with negligible capacity loss even after bending. This proves that the combination with MXenes can greatly improve the stability of the material. Hong [91] found a strong Co-O-Ti covalent interaction in

CoSe₂@MXene. It assembled the inner hollow CoSe₂ microsphere and the outer MXene via electrostatic self-assembly. This covalent bond facilitates electron/ion transport and enhances the structural durability of the CoSe₂@MXene hybrid, thus improving the rate performance and cyclic stability. It has been reported that the polar surface of MXenes can inhibit the polysulfides' shuttle effect [125,126]. Wang [127] was therefore inspired to grow CoSe₂ nanorods in situ on the surface of an MXene via a simple one-step hydrothermal method. Importantly, the stability of the CoSe₂/MXene cycle in this study was better than that of the pure CoSe₂ cycle, demonstrating that Ti₃C₂T_x can inhibit the undervoltage failure caused by Na_xSe instability.

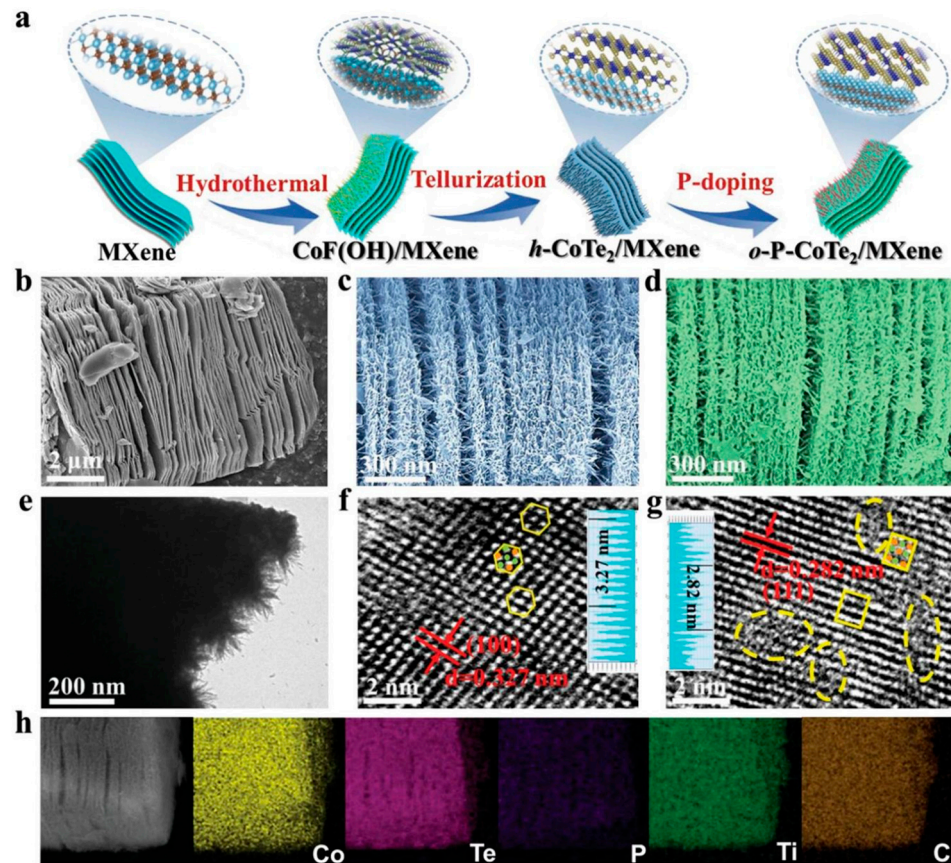


Figure 11. (a) Preparation process. SEM images of (b) MXene, (c) h-CoTe₂/MXene, and (d) o-P-CoTe₂/MXene. (e,g) TEM and HRTEM images of o-P-CoTe₂/MXene; (f) HRTEM of h-CoTe₂/MXene. (h) EDS spectrum of o-P-CoTe₂/MXene; Ref. [38].

3.3. Summary of Electrode Design

Cobalt selenide, as a high-capacity conversion anode, has been widely studied in alkali-metal-ion batteries. The new electrode design methods, such as doping with composite conductive materials (e.g., MXenes), can show excellent high capacity and high stability. However, the wide application and innovation of cobalt selenide in potassium-ion batteries still need to be improved. Cobalt telluride, as a compound of the same series, is still in its infancy in the design of advanced anode materials. Some novel designs of cobalt telluride show excellent electrochemical performance, which indicates the great potential of cobalt telluride. However, innovative designs of cobalt selenide are still to be developed; for example, co-doping with multiple non-metallic elements, carbon cloth growth, and electrospinning in situ growth methods have not been tried. At the same time, the electrochemical reaction mechanism of various synergistic effects is still unclear, and products with ultra-long periods of stability are still to be developed.

4. Electrode Synthesis

In addition to the elemental composition of the material, the morphology, crystal phase, and structure of the material also have a great influence on its properties. The microstructure of materials, such as their size and morphology, will affect their electron energy density, as well as influencing their optical and electrical properties [90,107,108,128]. Therefore, choosing appropriate preparation methods to synthesize materials with special structures is the key to improving the properties of the materials. Conventional preparation methods of cobalt-based anode materials include, but are not limited to, hydrothermal/solvothermal methods [32,101,113,116], heat treatment methods [52,93,129], sol-gel methods [130], vapor deposition methods [34], and electrospinning [100]. At the same time, the usual method for preparing selenides and tellurides is the gas-phase method [34].

Hydrothermal reaction is a typical synthesis route. Under certain temperature and high-pressure conditions, cobalt-based materials with high phase purity and crystallinity can be synthesized. For example, Lei et al. [131] synthesized uniform CoTe_2 nanorods by the hydrothermal method, without any surfactant or mineralizer for 20 h, using ascorbic acid as a reducing agent. The study found that simply adjusting the concentration of sodium hydroxide can produce different forms, including short rod-shaped bodies with many spines and flower-like hierarchies (Figure 12a–f). Hydrothermal methods are widely used in the synthesis of various materials, due to their advantages of fewer experimental steps, changeable morphology, and simple operation. However, hydrothermal methods also have some shortcomings, such as too many uncontrollable factors, easily leading to an uneven appearance, and a generally long hydrothermal reaction time. As a high-temperature treatment, the vapor-phase method can be used alone or in combination with a template method for intermediate processes such as selenides and tellurides. Cobalt-based electrode materials with an abundant pore structure and high electrochemical performance can be obtained by heat treatment. Heat treatment is almost a necessary experimental method for MOF-series materials, but this method has high energy consumption, and for MOF materials the sintering temperature is too high, which can easily lead to the collapse of the structure. The above methods are conducive to the formation of high-functional structures for $\text{CoSe}_x/\text{CoTe}_x$, but high-temperature pyrolysis is always necessary in the process of in situ carbonization. To achieve energy savings and high yields, it is urgent to explore more effective modification or combination methods such as magnetron sputtering [132], microwave [133], and molten salt etching [96,134] methods. The next section summarizes the current $\text{CoSe}_x/\text{CoTe}_x$ anode synthesis methods for LIBs, SIBs, and PIBs.

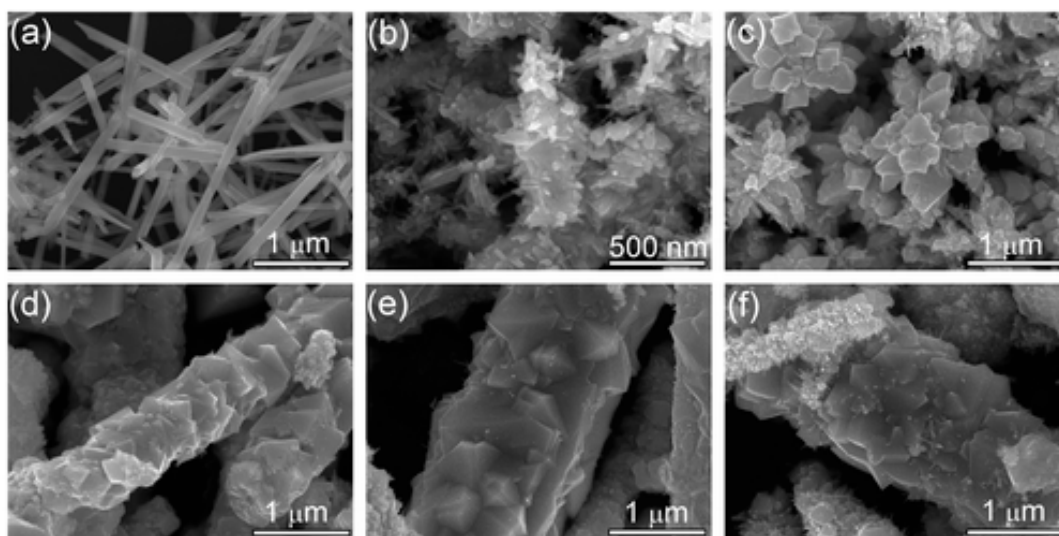


Figure 12. (a–f) SEM for CoTe_2 synthesized with different NaOH concentrations: 0.0 M, 0.2 M, 0.5 M, 1.2 M, 1.5 M, and 2.0 M. Ref. [131].

5. Performance Summary

This section focuses on the latest advances in the synthesis of various cobalt-based selenides and tellurides for LIBs, SIBs, and PIBs, and it summarizes the key properties and synthesis methods of various heterostructured anodes, as shown in the following Tables 1 and 2.

Table 1. Review of the properties of CoSe_x electrode materials.

Sample Name	Synthesis Method	Structure	Cycle Performance (mAh g ⁻¹ , A g ⁻¹)	Rate Performance (mAh g ⁻¹ , A g ⁻¹)	Initial Coulombic Efficiency (%), A g ⁻¹)	Battery Type	Ref./Year
CoSe ₂ /carbon nanoboxes	Annealing	Nanoboxes	860/0.2/100 th 660/1/100 th	686/2	78.3%/0.2	LIB	[135]/2016
CoSe@NCNTs	Annealing	Nanowires	326/0.5/100 th	278/3	95%/0.1	PIB	[18]/2021
CoSe ₂ -CNS	Annealing	Nanosheets	~250/10/2000 th	352/10		SIB	[103]/2019
CoSe ₂ @NC/CNTs	Annealing	Nanowires	480/1/200 th 369/10/800 th	360/10		SIB	[136]/2022
Mo-CoSe ₂ @NC	Electrodeposition + selenization	Self-supporting nanosheet	672/0.5/200 th	313/5	47.9%/0.5	SIB	[68]/2022
In ₂ Se ₃ /CoSe ₂ -450	Annealing	MIL-68@ZIF-67 core-shell	445.0/0.5/200 th 297.5/5/2000 th 205.5/10/2000 th	371.6/20	61.2%/0.1	SIB	[39]/2021
TNC-CoSe ₂	Precipitation + sol-gel + annealing	Microcubes	511.2/0.2/200 th	464/6.4	88.26%/0.2	SIB	[130]/2021
ZnSe/CoSe ₂ -CN	Annealing	Spherical particles	547.1/0.5/300 th 422.6/3/300 th	362.1/20	97.7%/0.1	SIB	[83]/2022
CoSe ₂ @MXene	Annealing	Porous hollow shell encapsulated by MXene nanosheets	910/0.2/100 th 1279/1/1000 th	465/5	71.9%/0.2	LIB	[91]/2020
Ni _{0.47} Co _{0.53} Se ₂	Solvothermal	Coral-like	321/2/2000 th	277/15	98.5%/0.1	SIB	[86]/2019
p-CoSeO ₃ -CNF	Electrospun + annealing	Composite porous nanofibers	288/0.2/200 th	207/5	56.7%/0.5	SIB	[100]/2021
CoSe ₂ /CoSe	Annealing	Hierarchical hollow raspberry-like superstructure	1361/1/1000 th 579/2/2000 th 315/5/1000 th	406/5		LIB	[54]/2019
Ni _{0.33} Co _{0.67} Se ₂	Solvothermal selenization	Hierarchical mesoporous nanospheres	301.9/1/1300 th	314.5/8	85.4%/0.5	SIB	[137]/2023
CoSe ₂ /ZnSe	Annealing	Bimetallic heterostructure	~250/8/4000 th ~200/10/4000 th	263/10	72.3%/0.1	SIB	[72]/2019
CoSSe@C/G	Solvothermal + annealing	Double-carbon shells	636.2/2/1400 th 353/1/200 th 208.1/0.2/100 th	254.5/10 266.6/10 195.7/2	68.09%/0.1 71.2%/0.1 48.3%/0.1	LIB SIB PIB	[33]/2020
NCNF@CS	Chemical vapor deposition + solvothermal	Octahedral threaded N-doped carbon nanotubes	253/0.2/100 th 173/2/600 th	196/2	69.3%/0.2	PIB	[34]/2018
3DG/CoSe ₂ @CNWs	Hydrogel	Multidimensional porous nanoarchitecture	543/0.1/100 302/2/500 th	~320/2	63.5%/0.1	SIB	[30]/2022

Table 1. Cont.

Sample Name	Synthesis Method	Structure	Cycle Performance (mAh g ⁻¹ , A g ⁻¹)	Rate Performance (mAh g ⁻¹ , A g ⁻¹)	Initial Coulombic Efficiency (%), A g ⁻¹)	Battery Type	Ref./Year
CoSe ₂ @NC/rGO-5	Two-step co-precipitation+ pyrolysis	Sandwich-like	527.5/0.1/100 th 226/0.5/400 th	206/5 157/10	72.6%/0.1	PIB	[138]/2021

Table 2. Review of the properties of CoTe_x electrode materials.

Sample	Synthesis Method	Structure	Cycle Performance ^x	Rate Performance (mAh g ⁻¹ , A g ⁻¹)	Initial Coulombic Efficiency (%), A g ⁻¹)	Battery Type	Ref./Year
CoTe ₂ -C	Annealing	Polyhedron	500/0.1/200 th 480/1/200 th	386/3	70.52%/0.1 56.07%/0.1	LIB SIB	[52]/2020
CoTe ₂ @3DG	Annealing	Polyhedron + rGO	191/0.05/350 th 103/1/4500 th	169/2	66.7%/0.05	SIB	[139]/2023
CoTe ₂ @NMCNFs	Electrospinning + annealing	Carbon fiber network	261.2/0.2/300 th 143.5/2/4000 th	152.4/10	57.1%/0.2	SIB	[47]/2021
CoTe ₂ @3DPNC	Annealing	Dual-type carbon	216.5/0.2/200 th	164.2/5	87.6%/0.2	SIB	[140]/2022
o-P-CoTe ₂ /MXene	Solvothermal annealing	MXene	373.7/0.2/200 th 232.3/2/2000 th	168.2/20	72.9%/0.05	PIB	[38]/2021
CTNRs/rGO	One-pot solvothermal	Nanorods/rGO	306/0.05/100 th	176/2	56%/0.05	SIB	[141]/2019
CoTe ₂ -C	Spray pyrolysis	Microsphere	295.8/0.2/100 th	163.7/2	69.2%/0.2	PIB	[142]/2020
Cu-Co _{1-x} Se ₂ @NC	Chemical etching tellurization	Hollow nanoboxes	796/1/800 th	~400/5	~80%/1	LIB	[71]/2022
CoTe ₂ /G	One-pot solvothermal	Nanosheets	356/0.05/100 th	246/5	78.1%/0.05	SIB	[42]/2018
ZnTe/CoTe ₂ @NC	Annealing	Bimetallic heterostructure	317.5/0.5/1000 th 254.5/2/2000 th 165.2/5/5000 th	190.2/5	58.3%/0.1	PIB	[40]/2022
o/h-CoTe ₂	One-step hydrothermal	Submicron-sized rods	807/0.12/200 th 438/0.6/400 th	305.8/3	75.2%/0.12	LIB	[93]/2023
CoTe@NCD	Simultaneous pyrolysis-tellurium melt impregnation	Carbon dodecahedra	300/0.1/100 th 200/0.1/100 th	207/2 58/2	57%/0.1 50%/0.05	SIB PIB	[129]/2022
CoTe ₂ @NPC-NFs@NC	Electrospinning	N-doped porous carbon nanofibers	409.1/0.05/50 th 198/0.5/600 th 120/2/1000 th	148.9/2	57.2%/0.05	PIB	[41]/2023

In general, cobalt selenide has been shown to be a high-energy anode for LIBs, SIBs, and PIBs, which greatly improves their electrochemical performance through independent electrodes without binders and with innovative heterojunction design. The reaction mechanism has also been studied by theoretical calculation and in situ techniques. As a potential electrode with high area capacity, cobalt telluride has many surprising applications in PIBs, and some electrode design methods that have proven excellent for cobalt selenide, such as heterojunctions and composite MXenes, have also been efficiently practiced for CoTe. However, compared with the metal oxides, sulfides, or selenides, the existing modification strategies are still insufficient. In addition, electrochemical performance can be enhanced by electrode synthesis and preparation. For example, studies on the compatibility of cobalt telluride with electrolytes and binders are still lacking. For practical applications, in future, more investigations and full battery evaluation should be emphasized.

6. Summary and Expectations

Cobalt selenide and cobalt telluride show promising applications in LIBs, SIBs, and PIBs due to their unique crystal structures, diverse structural designs, and high theoretical capacities. In this review, the progress of CoSe and CoTe was comprehensively summarized, not only focusing on the running mechanism and electrochemical performance, but also putting forward challenges to the synthesis strategies. The mechanism of Co-based chalcogenides in energy storage reactions is complex because it may have mechanisms for multilevel transformation. Often, conversion reactions are indispensable, which can lead to high weight capacities. However, disadvantages remain, such as large volume expansion and sluggish kinetics. In response to this series of problems, effective improvement strategies have been reported, including the design of nanocomposite carbon materials and the introduction of defects. Firstly, 0–3D conductive carbon nanocomposites can improve conductivity, create abundant active sites, and enhance electrolyte penetration. In addition, the introduced vacancies and heterogeneous interfaces can accelerate the conduction of ions and electrons. Tables 1 and 2 summarize the latest modified properties and synthesis methods, which can provide a reference point for innovative strategies for cobalt selenide and cobalt telluride materials. Nevertheless, the application of cobalt selenide and cobalt telluride anode materials in alkali-metal-ion batteries still requires extensive efforts. Therefore, we propose some prospective directions to promote further research to enable cobalt selenide and cobalt telluride to achieve higher energy storage efficiency.

6.1. Replenishing Existing Strategies

Heteroatom doping is an effective strategy to increase the numbers of ion storage locations and ion mobility channels, thereby facilitating faster electron transport. However, it is often reported that only one metallic element or non-metallic element (such as the common elements S and P) is selected to be mixed into cobalt selenide or cobalt telluride. At the same time, to improve the conductivity and active sites of CoSe_x and CoTe_x , the selection of composite carbon materials has been limited to traditional carbon materials, such as rGO, dopamine, super-C, or metal–organic frameworks. In addition, many reports testify that MXenes have the advantages of large interlayer spacing, good conductivity, and heteroatom doping. In summary, the new strategy of multi-element doping and synthesis and the novel MXene composite method can improve the performance of cobalt telluride and cobalt selenide as anodes for alkali-ion batteries.

6.2. Expanded CBs' Anode Material Synthesis Method

Compared to CoO_x and CoS_x , the available modification strategies are still limited. Currently, constructed multilayer, porous, or three-dimensional mesh structures can provide short transmission channels and large specific surface areas with active sites. This helps to improve material toughness and electrolyte contact, thus improving long-cycle performance. Relevant synthesis methods have been reported for CoSe_x , but less often for CoTe_x . Based on this, we should further explore the latter's electrochemical performance in LIBs/SIBs/PIBs. For example, three-dimensional nanonetworks of CoTe_x based on hydrogels may be a good synthesis method. Furthermore, binder-free electrodes for CoTe_x are rarely reported. Independent electrodes can be prepared via carbon cloth chemical deposition and electrospinning to avoid the obstruction of poor-conducting binders and low-capacity conductive agents, thus saving resources, reducing impurities, and improving the energy density.

Author Contributions: Writing—review and editing, Y.Z.; supervision, Z.S. and D.Q.; resources, D.H. and L.N. All authors have read and agreed to the published version of the manuscript.

Funding: This work was financially supported by the National Natural Science Foundation of China (22204028, 22104021, 22204159), Young Talent Support Project of Guangzhou Association for Science and Technology (QT-2023-003), Guangdong Basic and Applied Basic Research Fund Project (2022A1515110451), Guangzhou University Graduate Student Innovation Ability Cultivation Fund-

ing Program (2022GDJC-M06), and Science and Technology Projects in Guangzhou (202201010245, 2023A03J0029).

Institutional Review Board Statement: Not applicable.

Informed Consent Statement: Not applicable.

Data Availability Statement: Not applicable.

Conflicts of Interest: The authors declare no conflict of interest.

References

1. Grey, C.P.; Hall, D.S. Prospects for Lithium-Ion Batteries and beyond—A 2030 Vision. *Nat. Commun.* **2020**, *11*, 6279. [[CrossRef](#)] [[PubMed](#)]
2. Huy, V.P.H.; So, S.; Kim, I.T.; Hur, J. Self-Healing Gallium Phosphide Embedded in a Hybrid Matrix for High-Performance Li-Ion Batteries. *Energy Storage Mater.* **2021**, *34*, 669–681. [[CrossRef](#)]
3. Zhang, X.; He, Q.; Xu, X.; Xiong, T.; Xiao, Z.; Meng, J.; Wang, X.; Wu, L.; Chen, J.; Mai, L. Insights into the Storage Mechanism of Layered VS₂ Cathode in Alkali Metal-Ion Batteries. *Adv. Energy Mater.* **2020**, *10*, 1904118. [[CrossRef](#)]
4. Sun, Y.; Wang, H.; Wei, W.; Zheng, Y.; Tao, L.; Wang, Y.; Huang, M.; Shi, J.; Shi, Z.C.; Mitlin, D. Sulfur-Rich Graphene Nanoboxes with Ultra-High Potassiation Capacity at Fast Charge: Storage Mechanisms and Device Performance. *ACS Nano* **2021**, *15*, 1652–1665. [[CrossRef](#)]
5. Hao, Q.; Jia, G.; Wei, W.; Vinu, A.; Wang, Y.; Arandiyani, H.; Ni, B.J. Graphitic Carbon Nitride with Different Dimensionalities for Energy and Environmental Applications. *Nano Res.* **2020**, *13*, 18–37. [[CrossRef](#)]
6. Kim, H.; Kim, M.J.; Yoon, Y.H.; Nguyen, Q.H.; Kim, I.T.; Hur, J.; Lee, S.G. Sb₂Te₃-TiC-C Nanocomposites for the High-Performance Anode in Lithium-Ion Batteries. *Electrochim. Acta* **2019**, *293*, 8–18. [[CrossRef](#)]
7. Xie, H.; Kalisvaart, W.P.; Olsen, B.C.; Luber, E.J.; Mitlin, D.; Buriak, J.M. Sn-Bi-Sb Alloys as Anode Materials for Sodium Ion Batteries. *J. Mater. Chem. A Mater.* **2017**, *5*, 9661–9670. [[CrossRef](#)]
8. Zhou, Y.; Sun, W.; Rui, X.; Zhou, Y.; Ng, W.J.; Yan, Q.; Fong, E. Biochemistry-Derived Porous Carbon-Encapsulated Metal Oxide Nanocrystals for Enhanced Sodium Storage. *Nano Energy* **2016**, *21*, 71–79. [[CrossRef](#)]
9. Xiao, Y.; Hwang, J.Y.; Belharouak, I.; Sun, Y.K. Na Storage Capability Investigation of a Carbon Nanotube-Encapsulated Fe_{1-x}S Composite. *ACS Energy Lett.* **2017**, *2*, 364–372. [[CrossRef](#)]
10. Zhao, Y.; Wang, L.P.; Sougrati, M.T.; Feng, Z.; Leconte, Y.; Fisher, A.; Srinivasan, M.; Xu, Z. A Review on Design Strategies for Carbon Based Metal Oxides and Sulfides Nanocomposites for High Performance Li and Na Ion Battery Anodes. *Adv. Energy Mater.* **2017**, *7*, 1601424. [[CrossRef](#)]
11. Hartmann, F.; Etter, M.; Cibir, G.; Liers, L.; Terraschke, H.; Bensch, W. Superior Sodium Storage Properties in the Anode Material NiCr₂S₄ for Sodium-Ion Batteries: An X-ray Diffraction, Pair Distribution Function, and X-ray Absorption Study Reveals a Conversion Mechanism via Nickel Extrusion. *Adv. Mater.* **2021**, *33*, 2101576. [[CrossRef](#)] [[PubMed](#)]
12. Park, C.; Samuel, E.; Joshi, B.; Kim, T.; Aldalbahi, A.; El-Newehy, M.; Yoon, W.Y.; Yoon, S.S. Supersonically Sprayed Fe₂O₃/C/CNT Composites for Highly Stable Li-Ion Battery Anodes. *Chem. Eng. J.* **2020**, *395*, 125018. [[CrossRef](#)]
13. Ni, J.; Sun, M.; Li, L. Highly Efficient Sodium Storage in Iron Oxide Nanotube Arrays Enabled by Built-In Electric Field. *Adv. Mater.* **2019**, *31*, e1902603. [[CrossRef](#)] [[PubMed](#)]
14. Wang, X.; Liu, Y.; Han, H.; Zhao, Y.; Ma, W.; Sun, H. Polyaniline Coated Fe₃O₄ Hollow Nanospheres as Anode Materials for Lithium Ion Batteries. *Sustain. Energy Fuels* **2017**, *1*, 915–922. [[CrossRef](#)]
15. Xiao, Y.; Miao, Y.; Hu, S.; Gong, F.; Yu, Q.; Zhou, L.; Chen, S. Structural Stability Boosted in 3D Carbon-Free Iron Selenide through Engineering Heterointerfaces with Se-P Bonds for Appealing Na⁺-Storage. *Adv. Funct. Mater.* **2022**, *33*, 2210042. [[CrossRef](#)]
16. Sun, Z.; Shi, W.; Chen, J.; Gu, Z.; Lai, S.; Gan, S.; Xie, J.; Li, Q.; Qu, D.; Wu, X.L.; et al. Engineering Honeycomb-like Carbon Nanosheets Encapsulated Iron Chalcogenides: Superior Cyclability and Rate Capability for Sodium Ion Half/Full Batteries. *Electrochim. Acta* **2022**, *431*, 141084. [[CrossRef](#)]
17. Sun, Z.; Wu, X.; Gu, Z.; Han, P.; Zhao, B.; Qu, D.; Gao, L.; Liu, Z.; Han, D.; Niu, L. Rationally Designed Nitrogen-Doped Yolk-Shell Fe₇Se₈/Carbon Nanoboxes with Enhanced Sodium Storage in Half/Full Cells. *Carbon* **2020**, *166*, 175–182. [[CrossRef](#)]
18. Liu, Y.; Deng, Q.; Li, Y.; Li, Y.; Zhong, W.; Hu, J.; Ji, X.; Yang, C.; Lin, Z.; Huang, K. CoSe@N-Doped Carbon Nanotubes as a Potassium-Ion Battery Anode with High Initial Coulombic Efficiency and Superior Capacity Retention. *ACS Nano* **2021**, *15*, 1121–1132. [[CrossRef](#)]
19. Li, X.; Han, Z.; Yang, W.; Li, Q.; Li, H.; Xu, J.; Li, H.; Liu, B.; Zhao, H.; Li, S.; et al. 3D Ordered Porous Hybrid of ZnSe/N-Doped Carbon with Anomalously High Na⁺ Mobility and Ultrathin Solid Electrolyte Interphase for Sodium-Ion Batteries. *Adv. Funct. Mater.* **2021**, *31*, 2106194. [[CrossRef](#)]
20. Ge, J.M.; Fan, L.; Wang, J.; Zhang, Q.; Liu, Z.; Zhang, E.; Liu, Q.; Yu, X.; Lu, B. MoSe₂/N-Doped Carbon as Anodes for Potassium-Ion Batteries. *Adv. Energy Mater.* **2018**, *8*, 1801477. [[CrossRef](#)]
21. Liu, Y.; Yang, C.; Li, Y.; Zheng, F.; Li, Y.; Deng, Q.; Zhong, W.; Wang, G.; Liu, T. FeSe₂/Nitrogen-Doped Carbon as Anode Material for Potassium-Ion Batteries. *Chem. Eng. J.* **2020**, *393*, 124590. [[CrossRef](#)]

22. Sun, D.; Liu, S.; Zhang, G.; Zhou, J. NiTe₂/N-Doped Graphitic Carbon Nanosheets Derived from Ni-Hexamine Coordination Frameworks for Na-Ion Storage. *Chem. Eng. J.* **2019**, *359*, 1659–1667. [[CrossRef](#)]
23. Park, G.D.; Kang, Y.C. Conversion Reaction Mechanism for Yolk-Shell-Structured Iron Telluride-C Nanospheres and Exploration of Their Electrochemical Performance as an Anode Material for Potassium-Ion Batteries. *Small Methods* **2020**, *4*, 2000556. [[CrossRef](#)]
24. Bao, S.J.; Li, Y.; Li, C.M.; Bao, Q.; Lu, Q.; Guo, J. Shape Evolution and Magnetic Properties of Cobalt Sulfide. *Cryst. Growth Des.* **2008**, *8*, 3745–3749. [[CrossRef](#)]
25. Wang, L.H.; Teng, X.L.; Qin, Y.F.; Li, Q. High Electrochemical Performance and Structural Stability of CoO Nanosheets/CoO Film as Self-Supported Anodes for Lithium-Ion Batteries. *Ceram. Int.* **2021**, *47*, 5739–5746. [[CrossRef](#)]
26. Ren, L.L.; Wang, L.H.; Qin, Y.F.; Li, Q. One-Pot Synthesized Amorphous Cobalt Sulfide with Enhanced Electrochemical Performance as Anodes for Lithium-Ion Batteries. *Front. Chem.* **2022**, *9*, 818255. [[CrossRef](#)] [[PubMed](#)]
27. Lyu, Y.; Wu, X.; Wang, K.; Feng, Z.; Cheng, T.; Liu, Y.; Wang, M.; Chen, R.; Xu, L.; Zhou, J.; et al. An Overview on the Advances of LiCoO₂ Cathodes for Lithium-Ion Batteries. *Adv. Energy Mater.* **2021**, *11*, 2000982. [[CrossRef](#)]
28. Xiang, X.; Zhang, K.; Chen, J. Recent Advances and Prospects of Cathode Materials for Sodium-Ion Batteries. *Adv. Mater.* **2015**, *27*, 5343–5364. [[CrossRef](#)]
29. Kim, W.; Shin, D.; Seo, B.; Chae, S.; Jo, E.; Choi, W. Precisely Tunable Synthesis of Binder-Free Cobalt Oxide-Based Li-Ion Battery Anode Using Scalable Electrothermal Waves. *ACS Nano* **2022**, *16*, 17313–17325. [[CrossRef](#)]
30. Xiao, Q.; Song, Q.; Zheng, K.; Zheng, L.; Zhu, Y.; Chen, Z. CoSe₂ Nanodots Confined in Multidimensional Porous Nanoarchitecture towards Efficient Sodium Ion Storage. *Nano Energy* **2022**, *98*, 107326. [[CrossRef](#)]
31. Zhou, Y.; Han, Y.; Zhang, H.; Sui, D.; Sun, Z.; Xiao, P.; Wang, X.; Ma, Y.; Chen, Y. A Carbon Cloth-Based Lithium Composite Anode for High-Performance Lithium Metal Batteries. *Energy Storage Mater.* **2018**, *14*, 222–229. [[CrossRef](#)]
32. Liu, J.; Liang, J.; Wang, C.; Ma, J. Electrospun CoSe@N-Doped Carbon Nanofibers with Highly Capacitive Li Storage. *J. Energy Chem.* **2019**, *33*, 160–166. [[CrossRef](#)]
33. Wang, C.; Zhang, B.; Xia, H.; Cao, L.; Luo, B.; Fan, X.; Zhang, J.; Ou, X. Composition and Architecture Design of Double-Shelled Co_{0.85}Se_{1-x}S_x@Carbon/Graphene Hollow Polyhedron with Superior Alkali (Li, Na, K)-Ion Storage. *Small* **2020**, *16*, e1905853. [[CrossRef](#)] [[PubMed](#)]
34. Yu, Q.; Jiang, B.; Hu, J.; Lao, C.Y.; Gao, Y.; Li, P.; Liu, Z.; Suo, G.; He, D.; Wang, W.; et al. Metallic Octahedral CoSe₂ Threaded by N-Doped Carbon Nanotubes: A Flexible Framework for High-Performance Potassium-Ion Batteries. *Adv. Sci.* **2018**, *5*, 1800782. [[CrossRef](#)]
35. Yang, E.; Ji, H.; Jung, Y. Two-Dimensional Transition Metal Dichalcogenide Monolayers as Promising Sodium Ion Battery Anodes. *J. Phys. Chem. C* **2015**, *119*, 26374–26380. [[CrossRef](#)]
36. Ni, W.; Li, X.; Shi, L.Y.; Ma, J. Research Progress on ZnSe and ZnTe Anodes for Rechargeable Batteries. *Nanoscale* **2022**, *14*, 9609–9635. [[CrossRef](#)]
37. Yang, S.H.; Park, S.K.; Park, G.D.; Lee, J.H.; Kang, Y.C. Conversion Reaction Mechanism of Ultrafine Bimetallic Co–Fe Selenides Embedded in Hollow Mesoporous Carbon Nanospheres and Their Excellent K-Ion Storage Performance. *Small* **2020**, *16*, e2002345. [[CrossRef](#)]
38. Xu, X.; Zhang, Y.; Sun, H.; Zhou, J.; Liu, Z.; Qiu, Z.; Wang, D.; Yang, C.; Zeng, Q.; Peng, Z.; et al. Orthorhombic Cobalt Ditelluride with Te Vacancy Defects Anchoring on Elastic MXene Enables Efficient Potassium-Ion Storage. *Adv. Mater.* **2021**, *33*, 2100272. [[CrossRef](#)]
39. Xiao, S.; Li, X.; Zhang, W.; Xiang, Y.; Li, T.; Niu, X.; Chen, J.S.; Yan, Q. Bilateral Interfaces in In₂Se₃–CoIn₂–CoSe₂ Heterostructures for High-Rate Reversible Sodium Storage. *ACS Nano* **2021**, *15*, 13307–13318. [[CrossRef](#)]
40. Zhang, C.; Li, H.; Zeng, X.; Xi, S.; Wang, R.; Zhang, L.; Liang, G.; Davey, K.; Liu, Y.; Zhang, L.; et al. Accelerated Diffusion Kinetics in ZnTe/CoTe₂ Heterojunctions for High Rate Potassium Storage. *Adv. Energy Mater.* **2022**, *12*, 2202577. [[CrossRef](#)]
41. Li, Q.; Peng, J.; Zhang, W.; Wang, L.; Liang, Z.; Wang, G.; Wu, J.; Fan, W.; Li, H.; Wang, J.; et al. Manipulating the Polytellurides of Metallic Telluride for Ultra-Stable Potassium-Ion Storage: A Case Study of Carbon-Confined CoTe₂ Nanofibers. *Adv. Energy Mater.* **2023**, *13*, 2300150. [[CrossRef](#)]
42. Zhang, G.; Liu, K.; Zhou, J. Cobalt Telluride/Graphene Composite Nanosheets for Excellent Gravimetric and Volumetric Na-Ion Storage. *J. Mater. Chem. A Mater.* **2018**, *6*, 6335–6343. [[CrossRef](#)]
43. Cho, J.S.; Won, J.M.; Lee, J.K.; Kang, Y.C. Design and Synthesis of Multiroom-Structured Metal Compounds–Carbon Hybrid Microspheres as Anode Materials for Rechargeable Batteries. *Nano Energy* **2016**, *26*, 466–478. [[CrossRef](#)]
44. Li, J.; Yan, D.; Lu, T.; Yao, Y.; Pan, L. An Advanced CoSe Embedded within Porous Carbon Polyhedra Hybrid for High Performance Lithium-Ion and Sodium-Ion Batteries. *Chem. Eng. J.* **2017**, *325*, 14–24. [[CrossRef](#)]
45. Yang, X.; Wang, S.; Yu, D.Y.W.; Rogach, A.L. Direct Conversion of Metal–Organic Frameworks into Selenium/Selenide/Carbon Composites with High Sodium Storage Capacity. *Nano Energy* **2019**, *58*, 392–398. [[CrossRef](#)]
46. Sun, Z.; Gu, Z.; Shi, W.; Sun, Z.; Gan, S.; Xu, L.; Liang, H.; Ma, Y.; Qu, D.; Zhong, L.; et al. Mesoporous N-Doped Carbon-Coated CoSe Nanocrystals Encapsulated in S-Doped Carbon Nanosheets as Advanced Anode with Ultrathin Solid Electrolyte Interphase for High-Performance Sodium-Ion Half/Full Batteries. *J. Mater. Chem. A Mater.* **2022**, *10*, 2113–2121. [[CrossRef](#)]
47. Zhang, W.; Wang, X.; Wong, K.W.; Zhang, W.; Chen, T.; Zhao, W.; Huang, S. Rational Design of Embedded CoTe₂ nanoparticles in Freestanding N-Doped Multichannel Carbon Fibers for Sodium-Ion Batteries with Ultralong Cycle Lifespan. *ACS Appl. Mater. Interfaces* **2021**, *13*, 34134–34144. [[CrossRef](#)]

48. Chen, Z.; Chen, M.; Yan, X.; Jia, H.; Fei, B.; Ha, Y.; Qing, H.; Yang, H.; Liu, M.; Wu, R. Vacancy Occupation-Driven Polymorphic Transformation in Cobalt Ditelluride for Boosted Oxygen Evolution Reaction. *ACS Nano* **2020**, *14*, 6968–6979. [[CrossRef](#)]
49. Fan, H.; Mao, P.; Sun, H.; Wang, Y.; Mofarah, S.S.; Koshy, P.; Arandiyan, H.; Wang, Z.; Liu, Y.; Shao, Z. Recent Advances of Metal Telluride Anodes for High-Performance Lithium/Sodium-Ion Batteries. *Mater. Horiz.* **2022**, *9*, 524–546. [[CrossRef](#)]
50. Jiang, Y.; Zou, G.; Hou, H.; Li, J.; Liu, C.; Qiu, X.; Ji, X. Composition Engineering Boosts Voltage Windows for Advanced Sodium-Ion Batteries. *ACS Nano* **2019**, *13*, 10787–10797. [[CrossRef](#)]
51. Jiang, Y.; Xie, M.; Wu, F.; Ye, Z.; Zhang, Y.; Wang, Z.; Zhou, Y.; Li, L.; Chen, R. Cobalt Selenide Hollow Polyhedron Encapsulated in Graphene for High-Performance Lithium/Sodium Storage. *Small* **2021**, *17*, 2102893. [[CrossRef](#)] [[PubMed](#)]
52. Ganesan, V.; Nam, K.H.; Park, C.M. Robust Polyhedral CoTe₂-C Nanocomposites as High-Performance Li-A Nd Na-Ion Battery Anodes. *ACS Appl. Energy Mater.* **2020**, *3*, 4877–4887. [[CrossRef](#)]
53. Park, S.; Park, S.; Mathew, V.; Sambandam, B.; Hwang, J.Y.; Kim, J. A New Tellurium-Based Ni₃TeO₆-Carbon Nanotubes Composite Anode for Na-Ion Battery. *Int. J. Energy Res.* **2022**, *46*, 16041–16049. [[CrossRef](#)]
54. Ge, P.; Li, S.; Xu, L.; Zou, K.; Gao, X.; Cao, X.; Zou, G.; Hou, H.; Ji, X. Hierarchical Hollow-Microsphere Metal-Selenide@Carbon Composites with Rational Surface Engineering for Advanced Sodium Storage. *Adv. Energy Mater.* **2019**, *9*, 1803035. [[CrossRef](#)]
55. Miao, Y.; Xiao, Y.; Hu, S.; Chen, S. Chalcogenides Metal-Based Heterostructure Anode Materials toward Na⁺-Storage Application. *Nano Res.* **2022**, *16*, 2347–2365. [[CrossRef](#)]
56. Banhart, F.; Kotakoski, J.; Krashennnikov, A.V. Structural Defects in Graphene. *ACS Nano* **2011**, *5*, 26–41. [[CrossRef](#)]
57. Dong, C.; Zhang, X.; Dong, W.; Lin, X.; Cheng, Y.; Tang, Y.; Zhao, S.; Li, G.; Huang, F. ZnO/ZnS Heterostructure with Enhanced Interfacial Lithium Adsorption for Robust and Large-Capacity Energy Storage. *Energy Environ. Sci.* **2022**, *15*, 4738–4747. [[CrossRef](#)]
58. Arandiyan, H.; Mofarah, S.S.; Sorrell, C.C.; Doustkhah, E.; Sajjadi, B.; Hao, D.; Wang, Y.; Sun, H.; Ni, B.J.; Rezaei, M.; et al. Defect Engineering of Oxide Perovskites for Catalysis and Energy Storage: Synthesis of Chemistry and Materials Science. *Chem. Soc. Rev.* **2021**, *50*, 10116–10211. [[CrossRef](#)]
59. Wang, Y.; Arandiyan, H.; Chen, X.; Zhao, T.; Bo, X.; Su, Z.; Zhao, C. Microwave-Induced Plasma Synthesis of Defect-Rich, Highly Ordered Porous Phosphorus-Doped Cobalt Oxides for Overall Water Electrolysis. *J. Phys. Chem. C* **2020**, *124*, 9971–9978. [[CrossRef](#)]
60. Wang, X.; Li, F.; Li, W.; Gao, W.; Tang, Y.; Li, R. Hollow Bimetallic Cobalt-Based Selenide Polyhedrons Derived from Metal-Organic Framework: An Efficient Bifunctional Electrocatalyst for Overall Water Splitting. *J. Mater. Chem. A Mater.* **2017**, *5*, 17982–17989. [[CrossRef](#)]
61. Fang, C.; Huang, Y.; Zhang, W.; Han, J.; Deng, Z.; Cao, Y.; Yang, H. Routes to High Energy Cathodes of Sodium-Ion Batteries. *Adv. Energy Mater.* **2016**, *6*, 1501727. [[CrossRef](#)]
62. Billaud, J.; Singh, G.; Armstrong, A.R.; Gonzalo, E.; Roddatis, V.; Armand, M.; Rojo, T.; Bruce, P.G. Na_{0.67}Mn_{1-x}Mg_xO₂ (0 ≤ x ≤ 0.2): A High Capacity Cathode for Sodium-Ion Batteries. *Energy Environ. Sci.* **2014**, *7*, 1387–1391. [[CrossRef](#)]
63. Narsimulu, D.; Kakarla, A.K.; Vamsi Krishna, B.N.; Shanthappa, R.; Yu, J.S. Nitrogen-Doped Reduced Graphene Oxide Incorporated Ni₂O₃-Co₃O₄@MoS₂ Hollow Nanocubes for High-Performance Energy Storage Devices. *J. Alloys Compd.* **2022**, *922*, 166131. [[CrossRef](#)]
64. Jana, J.; Sharma, T.S.K.; Chung, J.S.; Choi, W.M.; Hur, S.H. The Role of Surface Carbide/Oxide Heterojunction in Electrocatalytic Behavior of 3D-Nanonest Supported FeiMoj Composites. *J. Alloys Compd.* **2023**, *946*, 169395. [[CrossRef](#)]
65. Pellow, M.A.; Emmott, C.J.M.; Barnhart, C.J.; Benson, S.M. Hydrogen or Batteries for Grid Storage? A Net Energy Analysis. *Energy Environ. Sci.* **2015**, *8*, 1938–1952. [[CrossRef](#)]
66. Ge, P.; Hou, H.; Li, S.; Huang, L.; Ji, X. Three-Dimensional Hierarchical Framework Assembled by Cobblestone-Like CoSe₂@C Nanospheres for Ultrastable Sodium-Ion Storage. *ACS Appl. Mater. Interfaces* **2018**, *10*, 14716–14726. [[CrossRef](#)]
67. Ge, P.; Hou, H.; Li, S.; Yang, L.; Ji, X. Tailoring Rod-Like FeSe₂ Coated with Nitrogen-Doped Carbon for High-Performance Sodium Storage. *Adv. Funct. Mater.* **2018**, *28*, 1801765. [[CrossRef](#)]
68. Lu, M.; Liu, C.; Li, X.; Jiang, S.; Yao, Z.; Liu, T.; Yang, Y. Mixed Phase Mo-Doped CoSe₂ Nanosheets Encapsulated in N-Doped Carbon Shell with Boosted Sodium Storage Performance. *J. Alloys Compd.* **2022**, *922*, 166265. [[CrossRef](#)]
69. Wang, M.Y.; Wang, X.L.; Yao, Z.J.; Xie, D.; Xia, X.H.; Gu, C.D.; Tu, J.P. Molybdenum-Doped Tin Oxide Nanoflake Arrays Anchored on Carbon Foam as Flexible Anodes for Sodium-Ion Batteries. *J. Colloid Interface Sci.* **2020**, *560*, 169–176. [[CrossRef](#)]
70. Wang, P.; Huang, J.; Zhang, J.; Wang, L.; Sun, P.; Yang, Y.; Yao, Z. Coupling Hierarchical Iron Cobalt Selenide Arrays with N-Doped Carbon as Advanced Anodes for Sodium Ion Storage. *J. Mater. Chem. A Mater.* **2021**, *9*, 7248–7256. [[CrossRef](#)]
71. Hu, L.; Li, L.; Zhang, Y.; Tan, X.; Yang, H.; Lin, X.; Tong, Y. Construction of Cobalt Vacancies in Cobalt Telluride to Induce Fast Ionic/Electronic Diffusion Kinetics for Lithium-Ion Half/Full Batteries. *J. Mater. Sci. Technol.* **2022**, *127*, 124–132. [[CrossRef](#)]
72. Fang, G.; Wang, Q.; Zhou, J.; Lei, Y.; Chen, Z.; Wang, Z.; Pan, A.; Liang, S. Metal Organic Framework-Templated Synthesis of Bimetallic Selenides with Rich Phase Boundaries for Sodium-Ion Storage and Oxygen Evolution Reaction. *ACS Nano* **2019**, *13*, 5635–5645. [[CrossRef](#)] [[PubMed](#)]
73. Ye, J.; Li, X.; Xia, G.; Gong, G.; Zheng, Z.; Chen, C.; Hu, C. P-Doped CoSe₂ Nanoparticles Embedded in 3D Honeycomb-like Carbon Network for Long Cycle-Life Na-Ion Batteries. *J. Mater. Sci. Technol.* **2021**, *77*, 100–107. [[CrossRef](#)]
74. Shin, I.; Cho, W.J.; An, E.S.; Park, S.; Jeong, H.W.; Jang, S.; Baek, W.J.; Park, S.Y.; Yang, D.H.; Seo, J.H.; et al. Spin-Orbit Torque Switching in an All-Van Der Waals Heterostructure. *Adv. Mater.* **2022**, *34*, e2101730. [[CrossRef](#)]

75. Pan, L.; Grutter, A.; Zhang, P.; Che, X.; Nozaki, T.; Stern, A.; Street, M.; Zhang, B.; Casas, B.; He, Q.L.; et al. Observation of Quantum Anomalous Hall Effect and Exchange Interaction in Topological Insulator/Antiferromagnet Heterostructure. *Adv. Mater.* **2020**, *32*, 2001460. [[CrossRef](#)] [[PubMed](#)]
76. Wang, H.; Niu, R.; Liu, J.; Guo, S.; Yang, Y.; Liu, Z.; Li, J. Electrostatic Self-Assembly of 2D/2D CoWO₄/g-C₃N₄ p-n Heterojunction for Improved Photocatalytic Hydrogen Evolution: Built-in Electric Field Modulated Charge Separation and Mechanism Unveiling. *Nano Res.* **2022**, *15*, 6987–6998. [[CrossRef](#)]
77. Huang, S.; Wang, Z.; von Lim, Y.; Wang, Y.; Li, Y.; Zhang, D.; Yang, H.Y. Recent Advances in Heterostructure Engineering for Lithium–Sulfur Batteries. *Adv. Energy Mater.* **2021**, *11*, 2003689. [[CrossRef](#)]
78. Li, Y.; Zhang, J.; Chen, Q.; Xia, X.; Chen, M. Emerging of Heterostructure Materials in Energy Storage: A Review. *Adv. Mater.* **2021**, *33*, 2100855. [[CrossRef](#)]
79. Liang, L.; Gu, W.; Wu, Y.; Zhang, B.; Wang, G.; Yang, Y.; Ji, G. Heterointerface Engineering in Electromagnetic Absorbers: New Insights and Opportunities. *Adv. Mater.* **2022**, *34*, 2106195. [[CrossRef](#)]
80. Wang, S.; Yang, Y.; Quan, W.; Hong, Y.; Zhang, Z.; Tang, Z.; Li, J. Ti³⁺-Free Three-Phase Li₄Ti₅O₁₂/TiO₂ for High-Rate Lithium Ion Batteries: Capacity and Conductivity Enhancement by Phase Boundaries. *Nano Energy* **2017**, *32*, 294–301. [[CrossRef](#)]
81. Luo, D.; Ma, C.; Hou, J.; Zhang, Z.; Feng, R.; Yang, L.; Zhang, X.; Lu, H.; Liu, J.; Li, Y.; et al. Integrating Nanoreactor with O–Nb–C Heterointerface Design and Defects Engineering Toward High-Efficiency and Longevous Sodium Ion Battery. *Adv. Energy Mater.* **2022**, *12*, 2103716. [[CrossRef](#)]
82. Yang, C.; Liang, X.; Ou, X.; Zhang, Q.; Zheng, H.S.; Zheng, F.; Wang, J.H.; Huang, K.; Liu, M. Heterostructured Nanocube-Shaped Binary Sulfide (SnCo)S₂ Interlaced with S-Doped Graphene as a High-Performance Anode for Advanced Na⁺ Batteries. *Adv. Funct. Mater.* **2019**, *29*, 1807971. [[CrossRef](#)]
83. Xiao, Y.; Miao, Y.; Wan, S.; Sun, Y.K.; Chen, S. Synergistic Engineering of Se Vacancies and Heterointerfaces in Zinc–Cobalt Selenide Anode for Highly Efficient Na-Ion Batteries. *Small* **2022**, *18*, 2202582. [[CrossRef](#)] [[PubMed](#)]
84. Saliba, D.; Ammar, M.; Rammal, M.; Al-Ghoul, M.; Hmadeh, M. Crystal Growth of ZIF-8, ZIF-67, and Their Mixed-Metal Derivatives. *J. Am. Chem. Soc.* **2018**, *140*, 1812–1823. [[CrossRef](#)] [[PubMed](#)]
85. Venna, S.R.; Jasinski, J.B.; Carreon, M.A. Structural Evolution of Zeolitic Imidazolate Framework-8. *J. Am. Chem. Soc.* **2010**, *132*, 18030–18033. [[CrossRef](#)]
86. He, Y.; Luo, M.; Dong, C.; Ding, X.; Yin, C.; Nie, A.; Chen, Y.; Qian, Y.; Xu, L. Coral-like Ni_xCo_{1-x}Se₂ for Na-Ion Battery with Ultralong Cycle Life and Ultrahigh Rate Capability. *J. Mater. Chem. A Mater.* **2019**, *7*, 3933–3940. [[CrossRef](#)]
87. Zhu, H.; Li, Z.; Xu, F.; Qin, Z.; Sun, R.; Wang, C.; Lu, S.; Zhang, Y.; Fan, H. Ni₃Se₄@CoSe₂ Hetero-Nanocrystals Encapsulated into CNT-Porous Carbon Interpenetrating Frameworks for High-Performance Sodium Ion Battery. *J. Colloid Interface Sci.* **2022**, *611*, 718–725. [[CrossRef](#)]
88. Zhang, K.; Park, M.; Zhou, L.; Lee, G.H.; Li, W.; Kang, Y.M.; Chen, J. Urchin-Like CoSe₂ as a High-Performance Anode Material for Sodium-Ion Batteries. *Adv. Funct. Mater.* **2016**, *26*, 6728–6735. [[CrossRef](#)]
89. Ko, Y.N.; Choi, S.H.; Kang, Y.C. Hollow Cobalt Selenide Microspheres: Synthesis and Application as Anode Materials for Na-Ion Batteries. *ACS Appl. Mater. Interfaces* **2016**, *8*, 6449–6456. [[CrossRef](#)]
90. Hu, J.-Z.; Liu, W.-J.; Zheng, J.-H.; Li, G.-C.; Bu, Y.-F.; Qiao, F.; Lian, J.-B.; Zhao, Y. Coral-like Cobalt Selenide/Carbon Nanosheet Arrays Attached on Carbon Nanofibers for High-Rate Sodium-Ion Storage. *Rare Met.* **2023**, *42*, 916–928. [[CrossRef](#)]
91. Hong, L.; Ju, S.; Yang, Y.; Zheng, J.; Xia, G.; Huang, Z.; Liu, X.; Yu, X. Hollow-Shell Structured Porous CoSe₂ Microspheres Encapsulated by MXene Nanosheets for Advanced Lithium Storage. *Sustain. Energy Fuels* **2020**, *4*, 2352–2362. [[CrossRef](#)]
92. Gu, X.; Zhang, L.; Zhang, W.; Liu, S.; Wen, S.; Mao, X.; Dai, P.; Li, L.; Liu, D.; Zhao, X.; et al. A CoSe–C@C Core-Shell Structure with Stable Potassium Storage Performance Realized by an Effective Solid Electrolyte Interphase Layer. *J. Mater. Chem. A Mater.* **2021**, *9*, 11397–11404. [[CrossRef](#)]
93. Fan, H.; Liu, C.; Lan, G.; Mao, P.; Zheng, R.; Wang, Z.; Liu, Y.; Sun, H. Uniform Carbon Coating Mediated Multiphase Interface in Submicron Sized Rodlike Cobalt Ditelluride Anodes for High-Capacity and Fast Lithium Storage. *Electrochim. Acta* **2023**, *439*, 141614. [[CrossRef](#)]
94. Nie, P.; Le, Z.; Chen, G.; Liu, D.; Liu, X.; Wu, H.B.; Xu, P.; Li, X.; Liu, F.; Chang, L.; et al. Graphene Caging Silicon Particles for High-Performance Lithium-Ion Batteries. *Small* **2018**, *14*, 1800635. [[CrossRef](#)]
95. Xu, H.; Cao, J.; Shan, C.; Wang, B.; Xi, P.; Liu, W.; Tang, Y. MOF-Derived Hollow CoS Decorated with CeO_x Nanoparticles for Boosting Oxygen Evolution Reaction Electrocatalysis. *Angew. Chem.* **2018**, *130*, 8790–8794. [[CrossRef](#)]
96. Huang, P.; Ying, H.; Zhang, S.; Zhang, Z.; Han, W.Q. In Situ Fabrication of MXene/CuS Hybrids with Interfacial Covalent Bonding via Lewis Acidic Etching Route for Efficient Sodium Storage. *J. Mater. Chem. A Mater.* **2022**, *10*, 22135–22144. [[CrossRef](#)]
97. Jin, T.; Han, Q.; Wang, Y.; Jiao, L. 1D Nanomaterials: Design, Synthesis, and Applications in Sodium–Ion Batteries. *Small* **2018**, *14*, 1703086. [[CrossRef](#)]
98. Nie, S.; Liu, L.; Liu, J.; Xie, J.; Zhang, Y.; Xia, J.; Yan, H.; Yuan, Y.; Wang, X. Nitrogen-Doped TiO₂–C Composite Nanofibers with High-Capacity and Long-Cycle Life as Anode Materials for Sodium-Ion Batteries. *Nanomicro Lett.* **2018**, *10*, 71. [[CrossRef](#)]
99. La Monaca, A.; Paolella, A.; Guerfi, A.; Rosei, F.; Zaghbi, K. Electrospun Ceramic Nanofibers as 1D Solid Electrolytes for Lithium Batteries. *Electrochem. Commun.* **2019**, *104*, 106483. [[CrossRef](#)]
100. Park, J.S.; Park, G.D.; Kang, Y.C. Exploration of Cobalt Selenite–Carbon Composite Porous Nanofibers as Anode for Sodium-Ion Batteries and Unveiling Their Conversion Reaction Mechanism. *J. Mater. Sci. Technol.* **2021**, *89*, 24–35. [[CrossRef](#)]

101. Li, F.; Li, L.; Yao, T.; Liu, T.; Zhu, L.; Li, Y.; Lu, H.; Qian, R.; Liu, Y.; Wang, H. Electrospinning Synthesis of Porous Carbon Nanofiber Supported CoSe₂ Nanoparticles towards Enhanced Sodium Ion Storage. *Mater. Chem. Phys.* **2021**, *262*, 124314. [[CrossRef](#)]
102. Lin, J.; Zhong, Z.; Wang, H.; Zheng, X.; Wang, Y.; Qi, J.; Cao, J.; Fei, W.; Huang, Y.; Feng, J. Rational Constructing Free-Standing Se Doped Nickel-Cobalt Sulfides Nanotubes as Battery-Type Electrode for High-Performance Supercapattery. *J. Power Sources* **2018**, *407*, 6–13. [[CrossRef](#)]
103. Xia, Z.; Sun, H.; He, X.; Sun, Z.; Lu, C.; Li, J.; Peng, Y.; Dou, S.; Sun, J.; Liu, Z. In Situ Construction of CoSe₂@vertical-Oriented Graphene Arrays as Self-Supporting Electrodes for Sodium-Ion Capacitors and Electrocatalytic Oxygen Evolution. *Nano Energy* **2019**, *60*, 385–393. [[CrossRef](#)]
104. Li, Z.; Zhang, J.; Lou, X.W.D. Hollow Carbon Nanofibers Filled with MnO₂ Nanosheets as Efficient Sulfur Hosts for Lithium-Sulfur Batteries. *Angew. Chem.* **2015**, *127*, 13078–13082. [[CrossRef](#)]
105. Xin, D.; He, S.; Han, X.; Zhang, X.; Cheng, Z.; Xia, M. Co-Doped 1T-MoS₂ Nanosheets Anchored on Carbon Cloth as Self-Supporting Anode for High-Performance Lithium Storage. *J. Alloys Compd.* **2022**, *921*, 166099. [[CrossRef](#)]
106. Wang, G.; Chen, J.; Cai, P.; Jia, J.; Wen, Z. A Self-Supported Ni-Co Perselenide Nanorod Array as a High-Activity Bifunctional Electrode for a Hydrogen-Producing Hydrazine Fuel Cell. *J. Mater. Chem. A Mater.* **2018**, *6*, 17763–17770. [[CrossRef](#)]
107. Liu, B.; Li, H.; Cao, B.; Jiang, J.; Gao, R.; Zhang, J. Few Layered N, P Dual-Doped Carbon-Encapsulated Ultrafine MoP Nanocrystal/MoP Cluster Hybrids on Carbon Cloth: An Ultrahigh Active and Durable 3D Self-Supported Integrated Electrode for Hydrogen Evolution Reaction in a Wide PH Range. *Adv. Funct. Mater.* **2018**, *28*, 1801527. [[CrossRef](#)]
108. Sun, T.; Huang, C.; Shu, H.; Luo, L.; Liang, Q.; Chen, M.; Su, J.; Wang, X. Porous NiCo₂S₄ Nanoneedle Arrays with Highly Efficient Electrocatalysis Anchored on Carbon Cloths as Self-Supported Hosts for High-Loading Li-S Batteries. *ACS Appl. Mater. Interfaces* **2020**, *12*, 57975–57986. [[CrossRef](#)]
109. Zeng, M.; Wang, M.; Zheng, L.; Gao, W.; Liu, R.; Pan, J.; Zhang, H.; Yang, Z.; Li, X. In Situ Enhance Lithium Polysulfides Redox Kinetics by Carbon Cloth/MoO₃ Self-Standing Electrode for Lithium-Sulfur Battery. *J. Mater. Sci.* **2022**, *57*, 10003–10016. [[CrossRef](#)]
110. Kim, I.; Park, S.W.; Kim, D.W. Carbon-Coated Tungsten Diselenide Nanosheets Uniformly Assembled on Porous Carbon Cloth as Flexible Binder-Free Anodes for Sodium-Ion Batteries with Improved Electrochemical Performance. *J. Alloys Compd.* **2020**, *827*, 154348. [[CrossRef](#)]
111. Li, T.; Bai, Y.; Wang, Y.; Xu, H.; Jin, H. Advances in Transition-Metal (Zn, Mn, Cu)-Based MOFs and Their Derivatives for Anode of Lithium-Ion Batteries. *Coord Chem. Rev.* **2020**, *410*, 213221. [[CrossRef](#)]
112. Wang, H.; Zhu, Q.L.; Zou, R.; Xu, Q. Metal-Organic Frameworks for Energy Applications. *Chem* **2017**, *2*, 52–80. [[CrossRef](#)]
113. Miao, W.; Zhang, Y.; Li, H.; Zhang, Z.; Li, L.; Yu, Z.; Zhang, W. ZIF-8/ZIF-67-Derived 3D Amorphous Carbon-Encapsulated CoS/NCNTs Supported on CoS-Coated Carbon Nanofibers as an Advanced Potassium-Ion Battery Anode. *J. Mater. Chem. A Mater.* **2019**, *7*, 5504–5512. [[CrossRef](#)]
114. Cheng, Z.; Du, T.; Gong, H.; Zhou, L. In-Situ Synthesis of Fe₇S₈ on Metal Sites of MOFs as High-Capacity and Fast-Kinetics Anodes for Sodium Ion Batteries. *J. Alloys Compd.* **2023**, *940*, 168854. [[CrossRef](#)]
115. Guo, W.; Sun, W.; Lv, L.P.; Kong, S.; Wang, Y. Microwave-Assisted Morphology Evolution of Fe-Based Metal-Organic Frameworks and Their Derived Fe₂O₃ Nanostructures for Li-Ion Storage. *ACS Nano* **2017**, *11*, 4198–4205. [[CrossRef](#)] [[PubMed](#)]
116. Zhang, Y.; Pan, A.; Ding, L.; Zhou, Z.; Wang, Y.; Niu, S.; Liang, S.; Cao, G. Nitrogen-Doped Yolk-Shell-Structured CoSe/C Dodecahedra for High-Performance Sodium Ion Batteries. *ACS Appl. Mater. Interfaces* **2017**, *9*, 3624–3633. [[CrossRef](#)]
117. Feng, J.; Luo, S.H.; Yan, S.X.; Zhan, Y.; Wang, Q.; Zhang, Y.H.; Liu, X.; Chang, L.J. Rational Design of Yolk-Shell Zn-Co-Se@N-Doped Dual Carbon Architectures as Long-Life and High-Rate Anodes for Half/Full Na-Ion Batteries. *Small* **2021**, *17*, e2101887. [[CrossRef](#)]
118. Yin, Y.; Rioux, R.M.; Erdonmez, C.K.; Hughes, S.; Somorjai, G.A.; Alivisatos, A.P. Formation of Hollow Nanocrystals through the Nanoscale Kirkendall Effect. *Science* **2004**, *304*, 711–714. [[CrossRef](#)]
119. Wang, B.; Miao, X.; Dong, H.; Ma, X.; Wu, J.; Cheng, Y.; Geng, H.; Li, C.C. In Situ construction of Active Interfaces towards Improved High-Rate Performance of CoSe₂. *J. Mater. Chem. A Mater.* **2021**, *9*, 14582–14592. [[CrossRef](#)]
120. Pang, J.; Mendes, R.G.; Bachmatiuk, A.; Zhao, L.; Ta, H.Q.; Gemming, T.; Liu, H.; Liu, Z.; Rummeli, M.H. Applications of 2D MXenes in Energy Conversion and Storage Systems. *Chem. Soc. Rev.* **2019**, *48*, 72–133. [[CrossRef](#)]
121. Yu, H.; Wang, Y.; Jing, Y.; Ma, J.; Du, C.F.; Yan, Q. Surface Modified MXene-Based Nanocomposites for Electrochemical Energy Conversion and Storage. *Small* **2019**, *15*, e1901503. [[CrossRef](#)] [[PubMed](#)]
122. Sun, H.; Zhang, Y.; Xu, X.; Zhou, J.; Yang, F.; Li, H.; Chen, H.; Chen, Y.; Liu, Z.; Qiu, Z.; et al. Strongly Coupled Te-SnS₂/MXene Superstructure with Self-Autoadjustable Function for Fast and Stable Potassium Ion Storage. *J. Energy Chem.* **2021**, *61*, 416–424. [[CrossRef](#)]
123. Kannan, K.; Sadasivuni, K.K.; Abdullah, A.M.; Kumar, B. Current Trends in MXene-Based Nanomaterials for Energy Storage and Conversion System: A Mini Review. *Catalysts* **2020**, *10*, 495. [[CrossRef](#)]
124. Nguyen, V.H.; Nguyen, B.S.; Hu, C.; Nguyen, C.C.; Nguyen, D.L.T.; Dinh, M.T.N.; Vo, D.V.N.; Trinh, Q.T.; Shokouhimehr, M.; Hasani, A.; et al. Novel Architecture Titanium Carbide (Ti₃C₂T_x) Mxene Cocatalysts toward Photocatalytic Hydrogen Production: A Mini-Review. *Nanomaterials* **2020**, *10*, 602. [[CrossRef](#)] [[PubMed](#)]
125. Ran, J.; Gao, G.; Li, F.T.; Ma, T.Y.; Du, A.; Qiao, S.Z. Ti₃C₂ MXene Co-Catalyst on Metal Sulfide Photo-Absorbers for Enhanced Visible-Light Photocatalytic Hydrogen Production. *Nat. Commun.* **2017**, *8*, 13907. [[CrossRef](#)] [[PubMed](#)]

126. Peng, Q.; Guo, J.; Zhang, Q.; Xiang, J.; Liu, B.; Zhou, A.; Liu, R.; Tian, Y. Unique Lead Adsorption Behavior of Activated Hydroxyl Group in Two-Dimensional Titanium Carbide. *J. Am. Chem. Soc.* **2014**, *136*, 4113–4116. [[CrossRef](#)]
127. Wang, M.; Peng, A.; Zeng, M.; Chen, L.; Li, X.; Yang, Z.; Chen, J.; Guo, B.; Ma, Z.; Li, X. Facilitating the Redox Conversion of CoSe₂ nanorods by Ti₃C₂T_x to Improve the Electrode Durability as Anodes for Sodium-Ion Batteries. *Sustain. Energy Fuels* **2021**, *5*, 6381–6391. [[CrossRef](#)]
128. Acharya, J.; Ojha, G.P.; Pant, B.; Park, M. Construction of Self-Supported Bimetallic MOF-Mediated Hollow and Porous Tri-Metallic Selenide Nanosheet Arrays as Battery-Type Electrodes for High-Performance Asymmetric Supercapacitors. *J. Mater. Chem. A Mater.* **2021**, *9*, 23977–23993. [[CrossRef](#)]
129. Sarkar, D.; Das, D.; Nagarajan, S.; Mitlin, D. Thermally Fabricated Cobalt Telluride in Nitrogen-Rich Carbon Dodecahedra as High-Rate Potassium and Sodium Ion Battery Anodes. *Sustain. Energy Fuels* **2022**, *6*, 3582–3590. [[CrossRef](#)]
130. Zhao, H.; Qi, Y.; Liang, K.; Li, J.; Zhou, L.; Chen, J.; Huang, X.; Ren, Y. Interface-Driven Pseudocapacitance Endowing Sandwiched CoSe₂/N-Doped Carbon/TiO₂ Microcubes with Ultra-Stable Sodium Storage and Long-Term Cycling Stability. *ACS Appl. Mater. Interfaces* **2021**, *13*, 61555–61564. [[CrossRef](#)]
131. Lei, Y.X.; Miao, N.X.; Zhou, J.P.; Hassan, Q.U.; Wang, J.Z. Novel Magnetic Properties of CoTe Nanorods and Diversified CoTe₂ Nanostructures Obtained at Different NaOH Concentrations. *Sci. Technol. Adv. Mater.* **2017**, *18*, 325–333. [[CrossRef](#)] [[PubMed](#)]
132. Keles, O.; Karahan, B.D.; Eryilmaz, L.; Amine, R.; Abouimrane, A.; Chen, Z.; Zuo, X.; Zhu, Z.; Al-Hallaj, S.; Amine, K. Superlattice-Structured Films by Magnetron Sputtering as New Era Electrodes for Advanced Lithium-Ion Batteries. *Nano Energy* **2020**, *76*, 105094. [[CrossRef](#)]
133. Sun, C.; Gao, L.; Yang, Y.; Yan, Z.; Zhang, D.; Bian, X. Ultrafast Microwave-Induced Synthesis of Lithiophilic Oxides Modified 3D Porous Mesh Skeleton for High-Stability Li-Metal Anode. *Chem. Eng. J.* **2023**, *452*, 139407. [[CrossRef](#)]
134. Huang, P.; Ying, H.; Zhang, S.; Zhang, Z.; Han, W.Q. Molten Salts Etching Route Driven Universal Construction of MX-ene/Transition Metal Sulfides Heterostructures with Interfacial Electronic Coupling for Superior Sodium Storage. *Adv. Energy Mater.* **2022**, *12*, 2202052. [[CrossRef](#)]
135. Hu, H.; Zhang, J.; Guan, B.; Lou, X.W.D. Unusual Formation of CoSe@carbon Nanoboxes, Which Have an Inhomogeneous Shell, for Efficient Lithium Storage. *Angew. Chem.* **2016**, *128*, 9666–9670. [[CrossRef](#)]
136. Sui, Y.; Guo, J.; Chen, X.; Guan, J.; Chen, X.; Wei, H.; Liu, Q.; Wei, B.; Geng, H. Highly Dispersive CoSe₂ Nanoparticles Encapsulated in Carbon Nanotube-Grafted Multichannel Carbon Fibers as Advanced Anodes for Sodium-Ion Half/Full Batteries. *Inorg. Chem. Front.* **2022**, *9*, 5217–5225. [[CrossRef](#)]
137. He, Y.; Li, H.; Yu, J.; Wang, Q.; Dai, Y.; Shan, R.; Zhou, G. Hierarchical Mesoporous Binary Nickel Cobalt Selenides Nanospheres for Enhanced Sodium-Ion Storage. *J. Alloys Compd.* **2023**, *938*, 168608. [[CrossRef](#)]
138. Zhao, J.; Wu, H.; Li, L.; Lu, S.; Mao, H.; Ding, S. A CoSe₂-Based 3D Conductive Network for High-Performance Potassium Storage: Enhancing Charge Transportation by Encapsulation and Restriction Strategy. *Mater. Chem. Front.* **2021**, *5*, 5351–5360. [[CrossRef](#)]
139. Jiang, Y.; Wu, F.; Ye, Z.; Zhou, Y.; Chen, Y.; Zhang, Y.; Lv, Z.; Li, L.; Xie, M.; Chen, R. Superimposed Effect of Hollow Carbon Polyhedron and Interconnected Graphene Network to Achieve CoTe₂ Anode for Fast and Ultralong Sodium Storage. *J. Power Sources* **2023**, *554*, 232174. [[CrossRef](#)]
140. Zhao, W.; Zhang, W.; Lei, Y.; Wang, L.; Wang, G.; Wu, J.; Fan, W.; Huang, S. Dual-Type Carbon Confinement Strategy: Improving the Stability of CoTe₂ Nanocrystals for Sodium-Ion Batteries with a Long Lifespan. *ACS Appl. Mater. Interfaces* **2022**, *14*, 6801–6809. [[CrossRef](#)]
141. Ding, Y.; Wang, W.; Bi, M.; Guo, J.; Fang, Z. CoTe Nanorods/RGO Composites as a Potential Anode Material for Sodium-Ion Storage. *Electrochim. Acta* **2019**, *313*, 331–340. [[CrossRef](#)]
142. Yang, S.; Park, G.D.; Kang, Y.C. Conversion Reaction Mechanism of Cobalt Telluride-Carbon Composite Microspheres Synthesized by Spray Pyrolysis Process for K-Ion Storage. *Appl. Surf. Sci.* **2020**, *529*, 147140. [[CrossRef](#)]

Disclaimer/Publisher's Note: The statements, opinions and data contained in all publications are solely those of the individual author(s) and contributor(s) and not of MDPI and/or the editor(s). MDPI and/or the editor(s) disclaim responsibility for any injury to people or property resulting from any ideas, methods, instructions or products referred to in the content.